

Pore-scale imaging with measurement of relative permeability and capillary pressure on the same reservoir sandstone sample under water-wet and mixed-wet conditions

Ying Gao ^{a,*}, Ali Q. Raeini ^a, Ahmed M. Selem ^a, Igor Bondino ^b, Martin J. Blunt ^a, Branko Bijeljic ^a

^a Department of Earth Science and Engineering, Imperial College London, London, United Kingdom

^b TOTAL E&P France, Pau, France



ARTICLE INFO

Keywords:

Micro-CT imaging
Relative permeability
Capillary pressure
Curvature
Wettability alteration
Pore occupancy

ABSTRACT

Using micro-CT imaging and differential pressure measurements, we design a comparative study in which we simultaneously measure relative permeability and capillary pressure on the same reservoir sandstone sample under water-wet and mixed-wet conditions during steady-state waterflooding experiments. This allows us to isolate the impact of wettability on a pore-by-pore basis and its effect on the macroscopic parameters, capillary pressure and relative permeability, while keeping the pore-space geometry unchanged.

First, oil and brine were injected through a water-wet reservoir sandstone sample at a fixed total flow rate, but in a sequence of increasing brine fractional flows with micro-CT scans of the fluid phases taken in each step. Then the sample was brought back to initial water saturation and the surface wettability of the sample was altered after prolonged contact with crude oil and the same measurement procedure was repeated on the altered-wettability sample which we call mixed-wet.

Geometric contact angles were measured, which discriminated the water-wet and mixed-wet cases with average values of 75° and 89° respectively. Additionally, an energy balance was used to determine the effective contact angles for displacement which indicated that a higher advancing contact angle of 116° was needed to displace oil in the mixed-wet case. For the water-wet experiment the filling sequence was pore-size dependent, with a strong correlation between pore size and oil occupancy. However, in the mixed-wet experiment the principal determinant of the filling sequence was the wettability rather than the pore size, and there was no correlation between pore size and the residual oil occupancy.

The oil-water interfacial area had a larger maximum in the mixed-wet case which was supported by the observation of sheet or saddle-like menisci shapes present throughout the sample volume that impede the flow. These shapes were quantified by much larger negative Gaussian curvature which indicated better connectivity of the phases, consistent with the lower residual oil saturation. Mean curvature and associated capillary pressure were positive for the water-wet case but decreased to a negative value for the mixed-wet case pointing to forced displacement from oil-wet pores. This analysis explained why the relative permeabilities for the mixed-wet case were lower than for the water-wet case for the same fractional flow.

1. Introduction

Multiphase flow in porous media is encountered in many geophysical and industrial applications, such as hydrocarbon recovery, carbon dioxide sequestration, groundwater management, and catalyst supports used in the automotive industry (Bachu, 2003; Blunt, 2017; Narula et al., 1996). To design these processes, an accurate understanding of the physics of flow at the underlying pore scale is of vital importance. In

particular, the important parameters affecting multiphase flow properties are wettability and pore-scale geometry.

The combination of X-ray computed microtomography (micro-CT), as an advanced imaging and analysis tool, as well as the use of high-pressure high-temperature coreflooding apparatus, provides a myriad of opportunities to develop insights into the fundamentals of multiphase flow in porous media. This methodology can provide not only measurements of capillary pressure (Andrew et al., 2014a; Armstrong et al., 2012) and relative permeability (Alhammadi et al., 2020; Gao et al., 2017) but also simultaneously includes a charac-

* Corresponding author.

E-mail address: y.gao15@imperial.ac.uk (Y. Gao).

terization of pore structure, contact angle, and curvature locally on a pore-by-pore basis (AlRatrou et al., 2017; Andrew et al., 2014b; Berg et al., 2013; Blunt et al., 2013; Herring et al., 2013; Khishvand et al., 2017; Saif et al., 2019; Wildenschild and Sheppard, 2013). More recently, it has been used to measure relative permeability and capillary pressure in water-wet and mixed-wet sandstones and carbonates (Alhammadi et al., 2020; Gao et al., 2017; Y., 2019; Lin et al., 2018; Q., 2019; Zou et al., 2018). However, hitherto there has not been a comparative study between water-wet and altered-wettability porous media with the same pore-space geometry that systematically relates local to macroscopic wettability descriptors of multiphase flow behaviour.

Wettability plays an important role in controlling the fluid configuration at the pore scale, which in turn impacts capillary pressure and relative permeability (Anderson, 1987a,b; Avraam and Payatakes, 1995, 1999; Blunt, 2017; Hirasaki, 1991). Since hydrocarbon reservoirs have been saturated with crude oil over geologic times, they are typically under altered-wettability conditions due to the deposition of surface-active components of the oil, asphaltenes, on the solid surface of the rock (Buckley et al., 1998; Kovsek et al., 1993; Salathiel, 1973). This wettability alteration changes the contact angle – the angle oil and water interface forms with the solid surface. Image-based measurements of contact angle inside the rock have shown that wettability cannot be described by a single contact angle (Alhammadi et al., 2017; AlRatrou et al., 2017). The wettability of the surface depends on the fluids, the surface itself, and the local pore geometry and roughness. This can result in a range of contact angle both above and below 90° – mixed-wet conditions – which can enable the simultaneous flow of oil and water over a wide range of saturations (AlRatrou et al., 2018). While the geometric contact angle, which directly measures this angle inside the rock from an image, can be used to characterise wettability, it does not necessarily describe the contact angle during fluid displacement (Akai et al., 2019). This is because the fluid-solid contacts are often pinned with a hinging angle; the contact only moves in a displacement when a sufficiently high, advancing angle, is reached that allows the water to progress across an oil-wet surface (Kovsek et al., 1993). The use of energy balance has provided a thermodynamic contact angle that captures the wettability consistent with the displacement observed (Akai et al., 2020; Blunt et al., 2019). In this work we will test both geometric and energy-balance approaches to understand wettability.

Zou et al. (2018) measured relative permeability in a mixed-wet Bentheimer sandstone with the wettability altered by an organic chemical, Octadecyltrichlorosilane (OTS), and compared these results with data obtained from the same sample under water-wet conditions. Lin et al. (2019) measured relative permeability and capillary pressure in mixed-wet Bentheimer and compared these to a water-wet case. Both these studies have found that the oil relative permeability was lower in the mixed-wet case before the crossover point (the saturation where the two relative permeabilities are equal) while the brine relative permeability was higher at the residual oil saturation. The low residual oil saturation observed in mixed-wet media implies that both oil and water remain connected through the pore space over a wide saturation range (Alhammadi et al., 2017; 2020; Lin et al., 2019). Topologically this is linked to the presence of saddle-shaped interfaces between oil and water with the two principal curvatures of different sign in orthogonal directions (Khanamiri et al., 2018). This results in a low capillary pressure but high connectivity of both oil and brine. Alhammadi et al. (2020) explored the relative permeability, capillary pressure and oil recovery in a mixed-wet microporous carbonate and observed saddle-shaped interfaces which helped explain the favourable oil recovery obtained. Moreover, the recovery was facilitated by water flowing through micro-porosity over a wide range of saturation, which was manifested through the low water relative permeability.

In a modelling study, Bakhshian et al. (2019) analysed the effect of wettability heterogeneity on a CO₂-brine system in a sandstone using the lattice Boltzmann method and found that, when the percentage of CO₂-wet regions increases at a given saturation for the

drainage cycle, the brine relative permeability is higher, the CO₂ relative permeability is lower, and the capillary pressure is lower. Furthermore, using the same method and for the same CO₂-brine system, Bakhshian et al. (2020) studied the interaction between wettability and heterogeneity for a wide range of contact angle (25°≤θ≤175°), and concluded that the both wettability and heterogeneity play an important role determining recovery.

These previous studies comparing water-wet and mixed-wet conditions were either performed on different samples or on the same sample but with wettability altered by a chemical instead of crude oil. To accurately assess and understand how crude oil alters wettability and how the wettability impacts fluid configurations and flow properties, it is necessary to perform both experiments on the same rock sample and use crude oil to mimic realistic reservoir conditions.

In this paper, we study oil and brine configurations in the pore space of the same reservoir sandstone sample under water-wet and mixed-wet conditions over a range of fractional flows. We use X-ray imaging combined with pressure measurements to quantify the impact that wettability alteration on a pore-by-pore basis exerts on pore and throat fluid occupancy and to relate these observations to the measured relative permeability and capillary pressure. Our goal is to quantify (i) geometric and thermodynamic contact angles, (ii) oil and brine pore occupancy and pore filling sequence, (iii) interfacial area, (iv) mean curvature, (v) Gaussian curvature, (vi) capillary pressure, and (vii) relative permeability. Using this rich range of multi-phase flow descriptors, we will accurately discriminate different wettability behaviour at the local (pore) and macroscopic (core) scales.

2. Materials and methods

2.1. Rock samples and fluid properties

A cylindrical sample of a reservoir sandstone, 6 mm in diameter with a length of 32 mm, was used in this study, as shown in Fig. 1. The porosity estimated from the micro-CT image was 0.184 ± 0.009, in which micro-porosity accounted for 0.022 ± 0.003. The micro-porosity was measured using differential imaging and will be characterised in Section 2.3.2. The helium porosity measured from a cm-scale sample from which this smaller sample was drilled was 0.206. Based on Darcy's law, the absolute permeability was calculated by measuring the pressure differential under single-phase (brine) flow to be 9.56(±0.06) × 10⁻¹³ m². The absolute permeability measured using the same method on the cm-sized rock from which our sample was taken was 9.8 × 10⁻¹³ m². The agreement for absolute permeability and porosity between the mm and cm-sized samples indicates that the rock is reasonably homogeneous at the mm-scale and that our results are likely to be representative of a larger body of rock.

The oil phase was Decalin with a dynamic viscosity of 2.96 ± 0.08 mPa·s at 20 °C (provided by Alfa Aesar). The aqueous (brine) phase was water doped with 3.5 wt% Potassium Iodide (KI), which was used as a high contrast dopant to distinguish the brine phase with the other two phases - oil and grain. The viscosity of the brine was 0.93±0.05 mPa·s measured by Rheometer MCR301 (Anton Paar), and the interfacial tension between oil and water was measured as 51.5 ± 1.6 mN/m by the pendant drop method using a Rame-Hart apparatus (590 F4 series) at ambient conditions (Andreas et al., 1938; Stauffer, 1965).

The crude oil used for ageing was from the oil field from which the sandstone sample was taken. The molecular weight was 229.3. The density and viscosity at 70 °C was 864.6 kg/m³ and 12.71 mPa·s respectively. The composition of the crude oil was 51 wt% saturates, 33.6 wt% aromatics and 15.4 wt% polar, measured by Total.

2.2. Experimental methods

This study consisted of three main experiments: a) a steady-state flow experiment performed on a water-wet sample in which the total flow

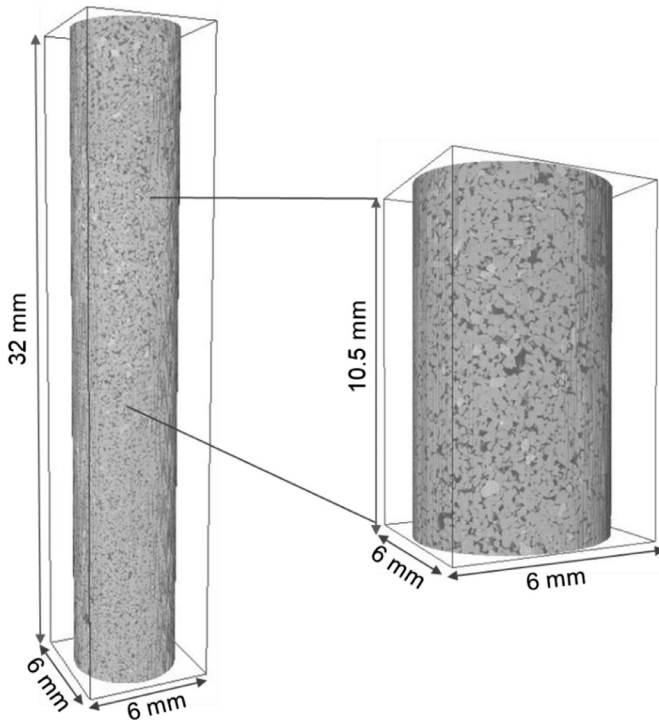


Fig. 1. On the left, the stitched three-dimensional X-ray image of the whole sample used in the experiment, with voxel size of 6 μm . On the right, the stitched highlighted smaller volume with voxel size of 3.58 μm . The dark is pore space and the grey is grain.

rate was 0.02 mL/min; b) wettability alteration at high temperature and high pressure on the same sample; and c) a steady-state flow experiment performed on the same sample now with altered wettability in which the total flow rate was again 0.02 mL/min.

The dual-injection flow apparatus used in this study is shown in Fig. 2. The experimental flow apparatus showing the three main components: core holder, differential pressure transducer, and four syringe pumps to apply a constant flow rate as well as confining and back pressure. The sample was placed in a fluoro-polymer elastomer (Viton) sleeve in the carbon fibre Hassler type flow cell. Fluid flow lines were used to connect the core holder with the pumps. Brine and oil were injected into the sample through two separate ports to ensure that two fluids flowed into the sample simultaneously. For the steady-state flow experiments, the total flow rate was 0.02 mL/min while varying the fractional flow, defined as the volumetric flow rate of water (brine) to the total flow rate (brine plus oil). The capillary number was 6.6×10^{-7} , based on the definition $Ca = \mu q / \sigma$, where μ is the average viscosity of the injected fluids, q is the total Darcy velocity, and σ is the interfacial tension between the two phases. This capillary number was chosen to ensure that fixed and stable brine and oil pathways could be observed, as shown in our previous work in Bentheimer sandstone (Gao et al., 2017; Gao et al., 2020).

The experiments were performed by following the steps:

1. The rock sample was put in the Viton sleeve in the core holder. Fluid flow lines were used to connect the pumps and core holder inside the micro-CT scanner.
2. Confining pressure was applied by injecting deionized water into the empty annulus space between the carbon fibre sleeve and the Viton sleeve. 2 MPa was set for confining pressure to avoid any bypass flow between the sample and the sleeve.
3. Four continuous images were taken for the whole sample with a voxel size of 6 μm . The overlap between one scan to the next was

approximately 25%. This overlap was used to stitch the two scans together. Two scans were taken over part of the sample with the voxel size of 3.58 μm . The scan position is shown in Fig. 1. The overlap between these two scans was about 25% as well.

4. Carbon dioxide was injected for 30 min to replace the air in the sample.
5. At least 200 pore volumes, PV, 30 wt% brine was injected into the rock sample to ensure that it was 100% saturated with brine. This step was used to measure the sub-resolution pore space, as the contrast between 30 wt% brine and grain was sufficient to observe the change in X-ray absorption in micro-porosity compared to the dry (air-saturated) scan (Lin et al., 2016; Gao et al., 2019; Alhammadi et al., 2020). This will be introduced in detail in Section 2.3.2.
6. The pressure differential between the inlet and outlet of the sample was measured over two flow rates, which was used to calculate the absolute permeability. A back pressure of 2 MPa was set for the flow system. The confining pressure was set at 4 MPa.
7. Four brine scans were taken for the whole sample when the voxel size was 6 μm and two more were taken when voxel size was 3.58 μm at the same positions as the dry scans.
8. At least 1000 PV 3.5 wt% brine was flooded to remove the high salinity brine in the sample.
9. At least 110 PV oil was injected from 0.02 mL/min to 2 mL/min to reach a uniform initial water saturation: this is a primary drainage process.
10. Oil was injected continually at a flow rate of 0.02 mL/min when the (brine) fractional flow was 0. When steady state was identified (the measured pressure drop was constant for more than 2 h), the scans were taken at the same position as mentioned in Step 3. It took approximately 24 h to reach steady state in this experiment.
11. Step 10 was repeated for fractional flows of $f_w = 0.05, 0.15, 0.3, 0.5, 0.7$ and 0.95 with a total flow rate of 0.02 mL/min. The oil flow rate was decreased from 0.019 mL/min to 0.001 mL/min and the brine flow rate was increased from 0.001 mL/min to 0.019 mL/min. Six scans were taken at each fractional flow at steady state at the same position as described in Step 3. The pressure differential was recorded throughout the whole experiment.
12. At least 110 PV brine was injected from 0.02 mL/min to 2 mL/min step by step to reach the residual oil saturation. Then brine injection continued at 0.02 mL/min to measure the pressure differential when the fractional flow was 1. Six scans were taken at the same position as described in Step 3.
13. The sample was taken out of the core holder and the pressure differences along the tubing were measured by repeating Steps 10 to 12 but without the rock present.
14. The brine in the sample was replaced by deionized water and dried in an oven for one week. Both water and remaining oil in the sample evaporated and left the sample clean and dry. Then the sample was put into the core holder and then moved into the oven. The oven temperature was $80 \pm 1^\circ\text{C}$.
15. Steps 1, 2, 4 and 8 were repeated. The pore pressure and confining pressure were set to 10 MPa and 12 MPa, respectively. The sandstone was kept at these conditions for 3 days to allow for ion equilibration occurring between the grains and brine.
16. At least 100 PV of heated crude oil (about 80°C) were injected into the sample from 0.02 mL/min to 2 mL/min. The sandstone sample was kept at these conditions for two weeks. Then the flow direction was reversed, and 100 more PV of crude oil were injected by increasing the flow rate from 0.02 mL/min to 2 mL/min. This was done to obtain a uniform initial brine saturation resulting in a homogeneous wettability alteration. The sample was then exposed to the same conditions for three more weeks. This whole process is called ageing and is used to alter the wettability of the sample, which mimics the reservoir conditions in the subsurface.

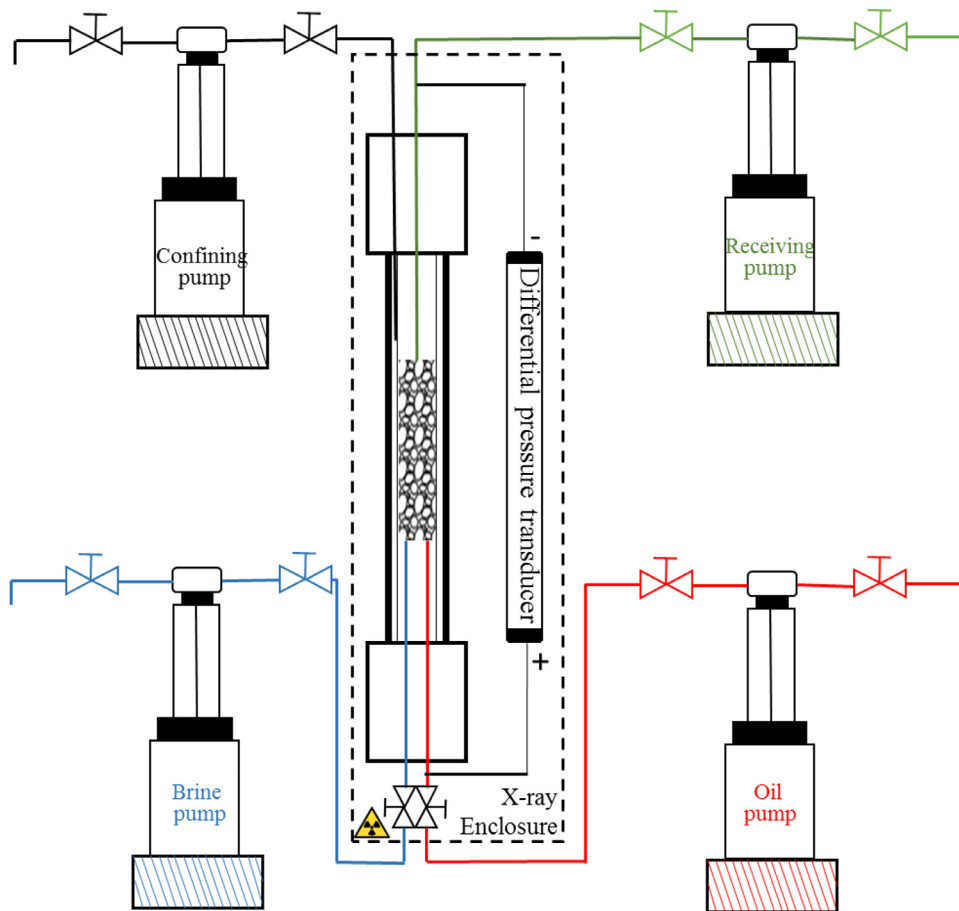


Fig. 2. The experimental flow apparatus showing the three main components: core holder, differential pressure transducer, and four syringe pumps to apply a constant flow rate as well as confining and back pressure.

17. The pore pressure was decreased to 2 MPa, and the confining pressure was decreased to 4 MPa. The core holder was then isolated by closing the valves connected to the tubing. Then the core holder was moved into the micro-CT scan with the apparatus as shown in Fig. 2. The PID controller was connected to the core holder and the temperature was set at 70 °C to allow the crude oil to flow.
18. Decalin was injected into the sample to displace the crude oil inside the sample until no crude oil was produced. Then the temperature was set back to ambient conditions.
19. Steps 9 to 12 were repeated on the mixed-wet sample. Oil and brine were co-injected at eight brine fractional flows ($f_w = 0, 0.05, 0.15, 0.3, 0.5, 0.7, 0.95$ and 1) at a fixed flow rate of 0.02 mL/min and images were taken at the same position as described in Step 3. Again, the pressure differential was recorded throughout the experiment.

2.3. Imaging methods and processing

2.3.1. Imaging method

The images were taken by a Zeiss XRM-510 X-ray microscope using a flat panel detector. The X-ray energy was 75 keV and the power was 6.5 W. The number of projections for each image was 2200 to enhance image quality. All tomograms were reconstructed into three-dimensional images using the Zeiss Reconstructor Software.

At each fractional flow, the four images with 6.35 μm voxel-size were normalized to the brine-saturated images, as a reference, and stitched together to obtain an image of the whole sample, as shown on the left in Fig. 1. The stitched image size was $1000 \times 1000 \times 5340$ voxels, which measured $6 \times 6 \times 32 \text{ mm}^3$. Similarly, each pair of overlapping images

with voxel size of 3.58 μm were normalized to the brine images and then stitched together, as shown on the right in Fig. 1. The stitched image size was $1608 \times 1608 \times 2933$ voxels, or $6 \times 6 \times 10.5 \text{ mm}^3$. All images were registered to the brine images to have the same orientation, and the Lanczos algorithm was used to resample the images (Burger and Burge, 2016). A non-local means filter was used to remove noise and smooth the images while preserving edges (Buades et al., 2005, 2008).

2.3.2. Characterization of the pore space

Differential imaging was used to quantify both the resolvable and the sub-resolution pore space. 30 wt% KI brine increased the contrast between brine and grain and emphasized the sub-resolution pore space (Lin et al., 2016). This was analysed from the $6 \times 6 \times 10.5 \text{ mm}^3$ sample with a voxel size of 3.58 μm . Fig. 3(A) shows a two-dimensional slice of the dry scan, while Fig. 3(B) shows the same slice of the fully brine-saturated image. We clearly observe some sub-resolution pores, with intermediate grey scales in both images, indicated by the yellow boxes. To quantify the porosity of the sub-resolution pore space, the differential image between Fig. 3(B) and (A) is obtained as shown in Fig. 3(C). Figs. 4 and 5 confirmed that oil did not enter these micro-porous regions during the steady-state experiments, proving that the capillary entry pressure was not sufficiently high for the oil to displace brine from these regions. Fig. 3(D) shows the segmented macro-pore space.

Table 1 lists the volume fraction of solid grain, micro-pore space, macro-pore space, and the corresponding porosity. The porosity of sub-resolution pores is 0.56 ± 0.01 and its contribution to the total porosity is 0.022 ± 0.003 , where the total porosity is 0.184 ± 0.009 . More details of this method can be found in Lin et al. (2016) and Gao et al. (2019).

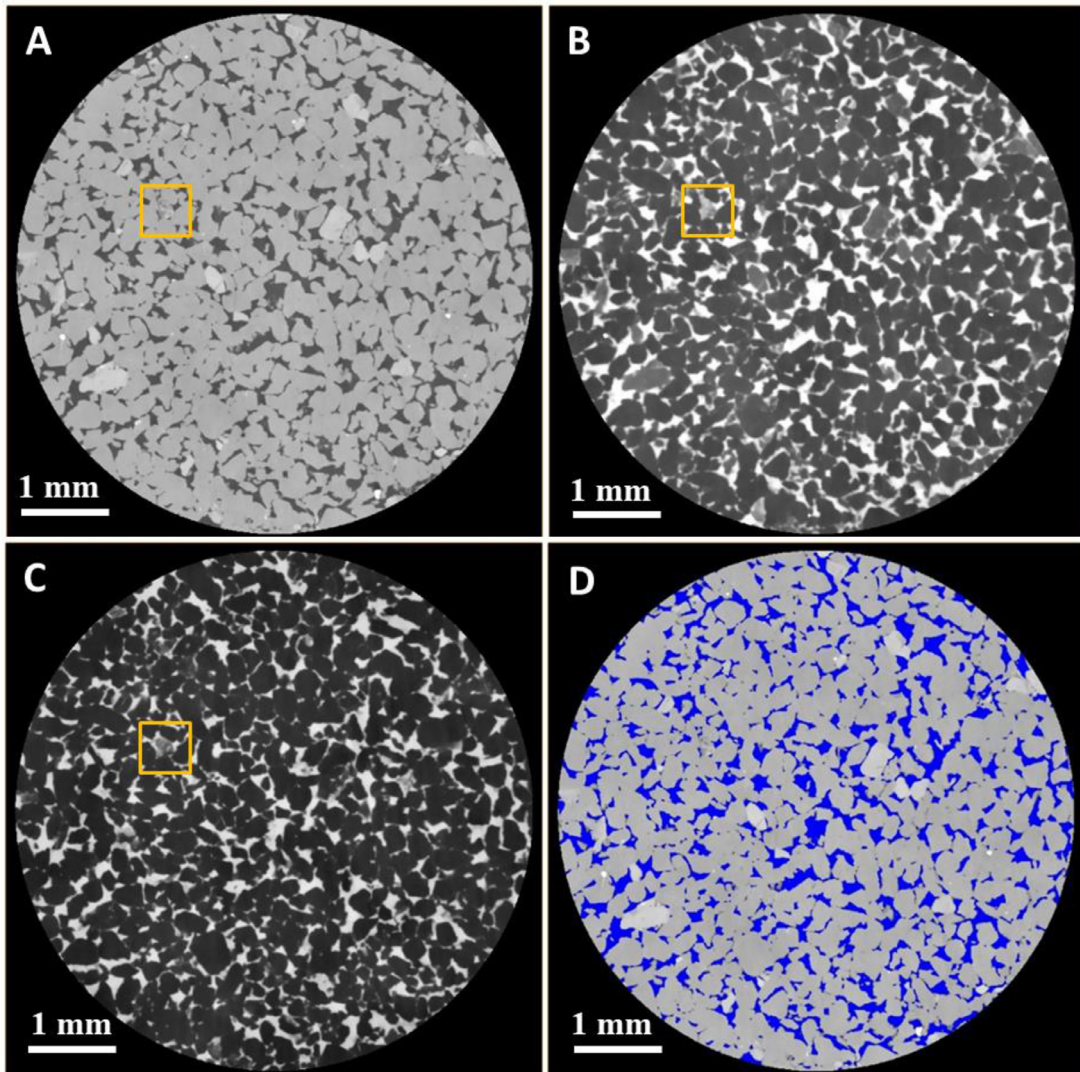


Fig. 3. Two-dimensional cross sections of three-dimensional micro-CT images. (A) An example of a dry scan. (B) Sample saturated with brine. (C) Difference image between (B) and (A). (D) Segmented pore space. The yellow boxes indicate regions containing micro-porosity.

Table 1

Volume fraction of solid grain, micro-pore space, macro-pore space, and the corresponding porosity for each phase, i.

Type	Volume fraction p_i	Porosity ϕ_i	Contribution to the total porosity $\phi_i = p_i \phi_i$
Solid grain	0.808	0	0
Micro-pore space	0.040	0.56	0.022 ± 0.003
Macro-pore space	0.162	1	0.162 ± 0.006
Total porosity	0.184 ± 0.009		

2.3.3. Characterization of fluids in the pore space

Grey-scale images for each fractional flow, with the voxel size of $3.58 \mu\text{m}$, from the water-wet experiment are illustrated in Fig. 4 while those from the mixed-wet experiment are shown in Fig. 5. The black is oil, the dark grey is grains and the light grey is brine.

The watershed method was applied to segment the images to oil and water phases (Beucher and Meyer, 1993). To quantify oil and brine saturation accurately, the images were cropped into cylindrical sections to avoid the sleeve shown at the boundary of the core. For the macro-pore space, the fluids were segmented into brine (blue) and oil (red), as shown in Fig. 6 (water-wet) and Fig. 7 (mixed-wet).

Table 2

Measurements and the corresponding image size and voxel size.

Measurement	Image size / mm^3	Voxel size / μm
Contact angle	$3.58 \times 3.58 \times 3.58$	3.58
Fluid occupancy	$3.58 \times 3.58 \times 3.58$	3.58
Interfacial area	$2 \times 2 \times 2$	3.58
Mean / Gaussian curvature	$2 \times 2 \times 2$	3.58
Capillary pressure	$2 \times 2 \times 2$	3.58
Relative permeability/ saturation	$6 \times 6 \times 32$	6.35

A description of the measurements used for this paper, which includes the image size and voxel size are listed in Table 2.

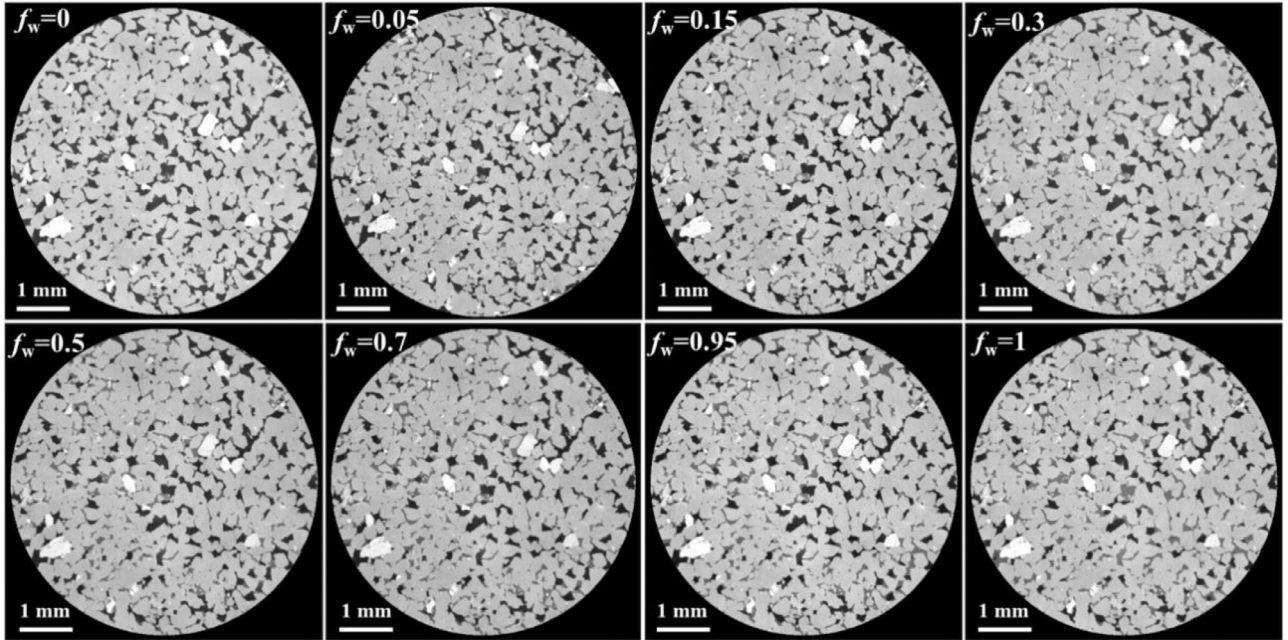


Fig. 4. Two-dimensional cross-sectional views of the three-dimensional X-ray images of the same slice at the eight fractional flows for the reservoir sandstone under water-wet conditions. The oil, rock and brine are shown in black, dark grey and light grey respectively.

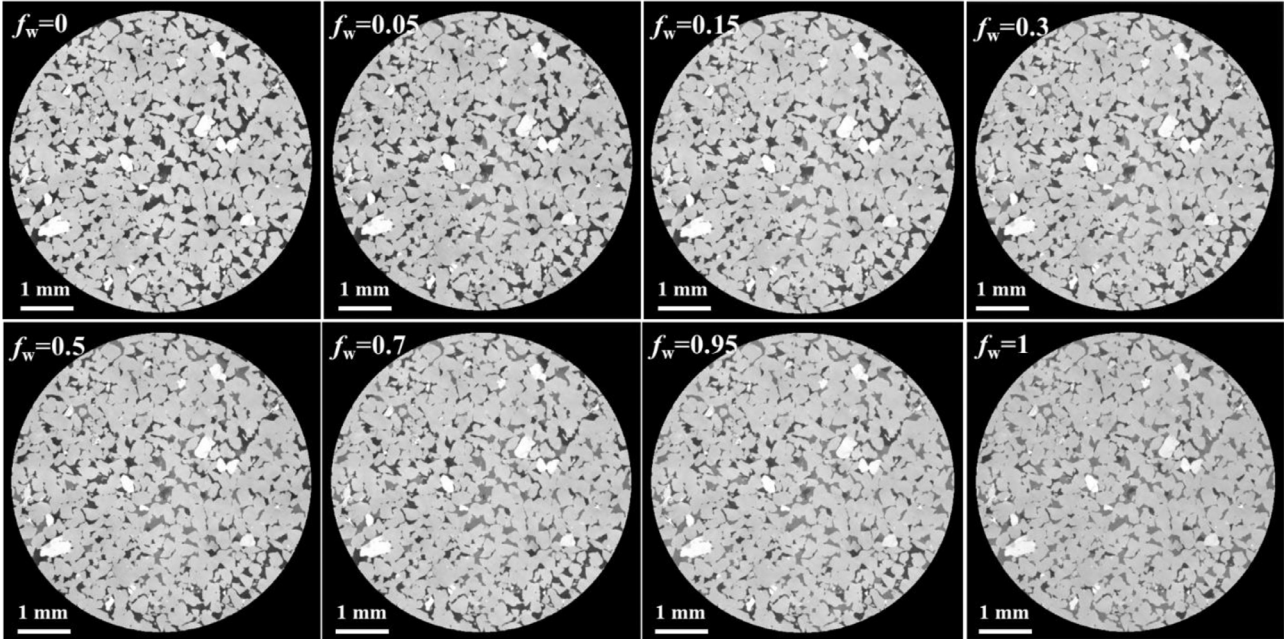


Fig. 5. Two-dimensional cross-sectional views of the three-dimensional X-ray images of the same slice at the eight fractional flows for the reservoir sandstone under mixed-wet conditions. The oil, rock and brine are shown in black, dark grey and light grey respectively.

3. Results and discussion

We start with wettability characterization by quantifying the geometric and thermodynamic contact angles for the two sets of experiments in [Section 3.1](#). Then we present fluid occupancy in pores and throats in [Section 3.2](#). This is followed by an analysis of interfacial area in [Section 3.3](#). In [Section 3.4](#), we present interfacial curvature, including mean curvature and Gaussian curvature. Then the calculation of capillary pressure from the mean curvature is described in [Section 3.5](#), followed by the determination of relative permeability in [Section 3.6](#).

3.1. Wettability characterization

[Fig. 8\(A\)](#) shows the configuration of oil and water in a selected region of the pore space under water-wet and mixed-wet conditions as an example. Black is oil and light grey is water. Oil resided in large pores under water-wet conditions, while it occupied some small pores and corners for the mixed-wet case.

In situ contact angle can be measured from X-ray images ([Alhammadi et al., 2017](#); [Andrew et al., 2014b](#)), and an automated method has been developed to quantify the distribution of contact an-

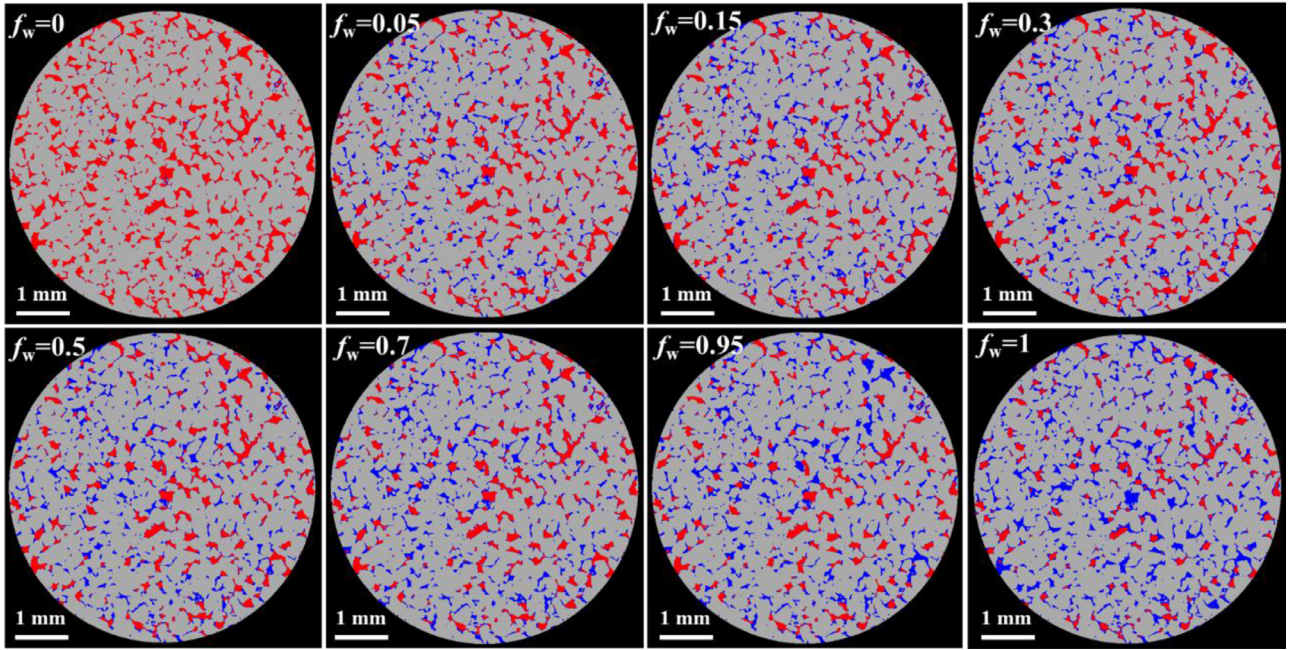


Fig. 6. Two-dimensional cross-sectional views of the three-phase segmented label image showing brine (blue), oil phase (red) and grain phase (grey) of the same slice at the eight fractional flows for the reservoir sandstone under water-wet conditions.

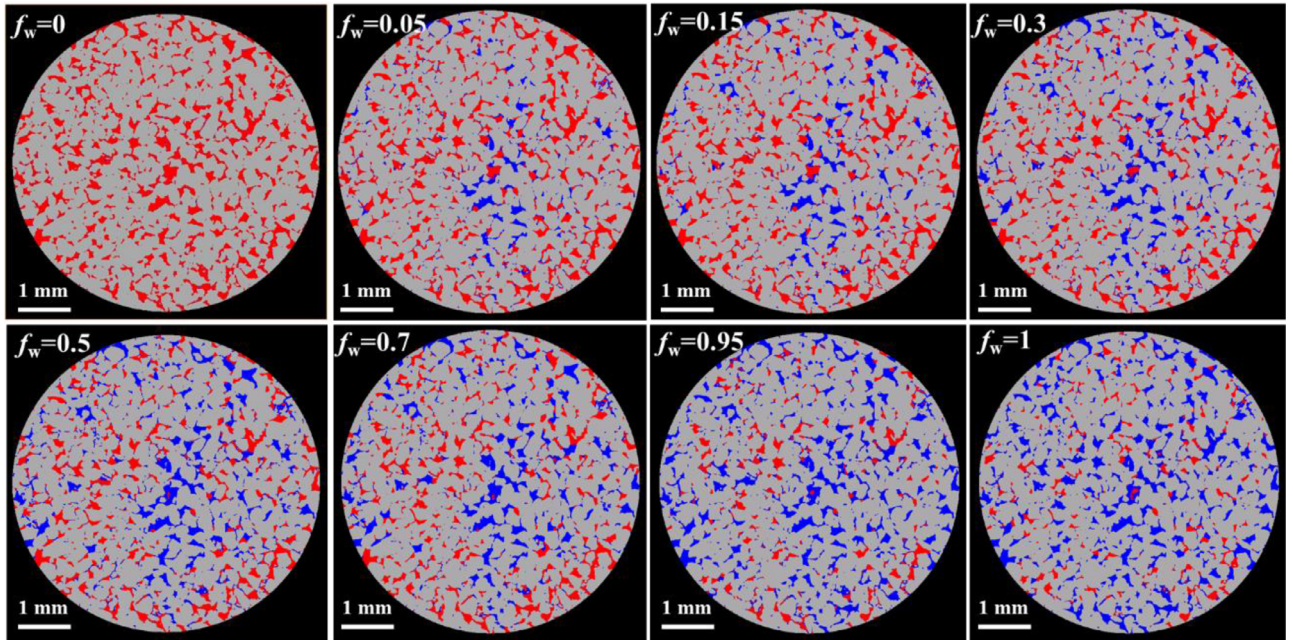


Fig. 7. Two-dimensional cross-sectional views of the three-phase segmented label image showing brine (blue), oil (red) and grain phase (grey) of the same slice at the eight fractional flows for the reservoir sandstone under mixed-wet conditions.

gle (AlRatrou et al., 2017): we call this the geometric contact angle. This automated method identifies the fluid-fluid and fluid-solid interfaces in the segmented images. These interfaces are then smoothed and the three-phase contact line, where the fluid-fluid interface contacts the solid, is identified. At every voxel in the image on the contact line, the two vectors that have a direction which is perpendicular to both surfaces (fluid-solid and fluid-fluid) is identified. Then contact angle values at all recognized oil-brine-solid contacts can be generated from the dot product of these vectors. We used this automated method to measure the distribution of contact angle when the fractional flow was 0.5, shown in Fig. 8(B).

The average contact angle was 74.9° and 88.8° for water-wet and mixed-wet conditions respectively. The geometric contact angle for all fractional flows under both conditions are listed in Table 3. We can see that there is a wider range of contact angles for mixed-wet case with values both above and below 90° . The wide range of measured contact angles reflects complex structure of the rough surfaces in the pore space (AlRatrou et al., 2018).

Because the geometric contact angle was measured directly at the three-phase contact line from the images, this process is particularly sensitive to the image quality and segmentation, which introduces uncertainties. Furthermore, because some interfaces between oil and brine

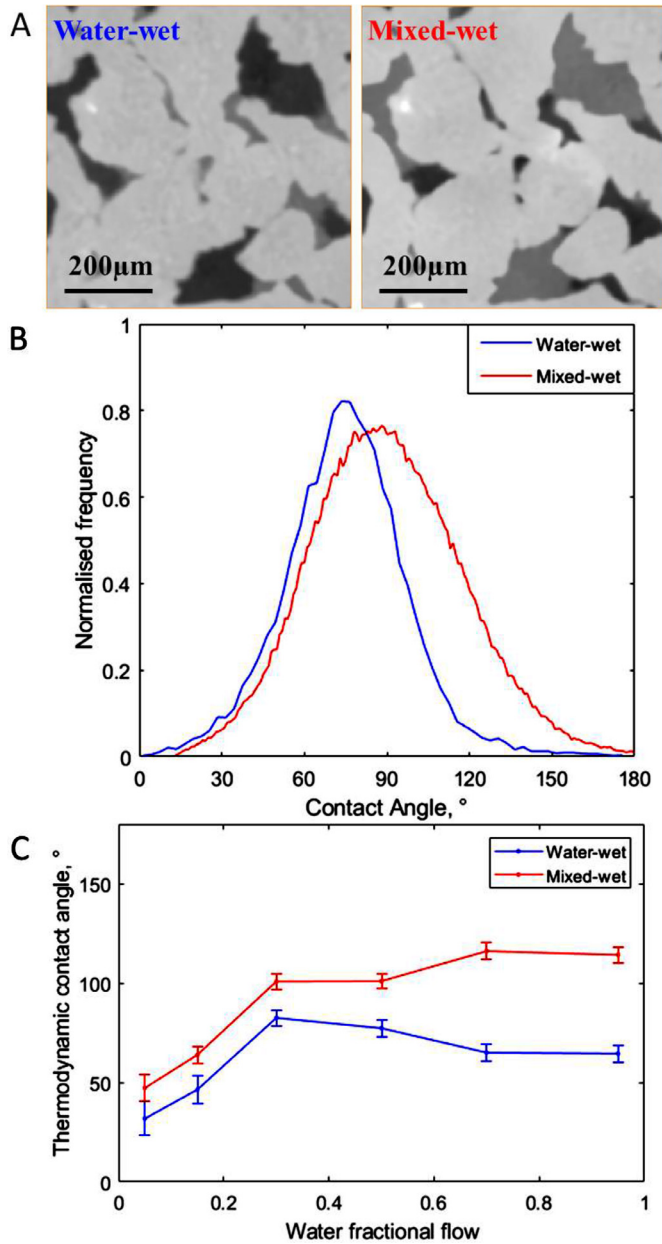


Fig. 8. (A) Examples of the oil and water distribution in the same region of pore space under water-wet (left) and mixed-wet (right) conditions. The oil, rock and brine are shown in black, dark grey and light grey respectively. (B) Histogram of the measured geometric in situ contact angle distribution on the segmented image when the fractional flow was 0.5 under both conditions. (C) Thermodynamic contact angle measured based on energy balance under both conditions and across different water fractional flow images.

Table 3

The geometric contact angle distribution showing the mean and standard deviation at eight fractional flows under both water-wet and mixed-wet conditions.

f_w	Contact angle / Water-wet	Contact angle / Mixed-wet
0.05	$76.3 \pm 26.1^\circ$	$88.2 \pm 25.4^\circ$
0.15	$74.8 \pm 21.9^\circ$	$88.6 \pm 25.2^\circ$
0.3	$73.6 \pm 20.5^\circ$	$88.7 \pm 25.7^\circ$
0.5	$74.9 \pm 22.1^\circ$	$88.8 \pm 27.4^\circ$
0.7	$74.1 \pm 20.1^\circ$	$89.7 \pm 28.6^\circ$
0.95	$76.1 \pm 21.0^\circ$	$88.6 \pm 26.4^\circ$
1	$74.3 \pm 20.8^\circ$	$90.8 \pm 27.3^\circ$

may be pinned at the contact line before a higher angle for brine to advance over an altered-wettability surface is reached (Morrow, 1970), the measured contact angles may not properly represent the values during a displacement.

To provide the wettability for a displacement process directly, the thermodynamic contact angle, considering changes in saturation and interfacial areas between each phase, are calculated from an energy balance assuming negligible viscous dissipation (Blunt et al., 2019):

$$\Delta a_{ws} \cos \theta_t = 2\kappa \phi \Delta S_w + \Delta a_{ow} \quad (1)$$

where Δa_{ws} is the change in the specific interfacial area between water (brine) and solid, θ_t is the thermodynamic contact angle, κ is the mean curvature, ϕ is the porosity, ΔS_w is the change in the water (brine) saturation and Δa_{ow} is the change in the specific interfacial area between oil and water (brine). The specific interfacial area here is defined as the surface area per unit volume.

Fig. 8(C) shows the thermodynamic contact angles calculated for water-wet and mixed-wet conditions. The differences in Eq. (1) are found from two subsequent fractional flows and the contact angle is shown as a function of the lower fractional flow used in the calculation. Up to $S_w = 0.3$ the contact angle increases to 100° in the mixed-wet case, and to 80° in the water-wet case. With further water injection, the thermodynamic contact angle increases to 116° in the mixed-wet case, while it slightly decreases to 65° in the water-wet experiment. A higher advancing contact angle is needed to displace oil in the mixed-wet case. As expected, brine first fills the more water-wet pores and then later less water-wet pores. More details on how interfacial area changes are provided in Section 3.3 and how the water saturation changes in Section 3.6.

3.2. Fluid occupancy in pores and throats

We now test how wettability impacts pore and throat occupancy from the segmented images previously shown in Figs. 6 and 7. The location and size of the pores and/or throats occupied by oil and brine are investigated. Based on the radii of spheres inscribed in the pore space, the void space was subdivided into pores representing wider regions and throats representing narrow connections between the pores using a generalized pore network extraction algorithm (Raeini et al., 2017). Each voxel is assigned to a unique pore as well as to a unique throat. The voxels, which are located at local maxima of the distance map (the distance of any point in the void space to the nearest solid), are assigned as the centres of pore or throat. Then the volume-weighted fraction of pores and throats whose centres were occupied by brine or oil were computed to analyse the statistics of the pore and throat fluid occupancy. Figs. 9 and 10 show the results for different fractional flows for the water-wet and mixed-wet experiments respectively.

For both cases, the initial water saturation was very low. Oil resided in almost all the pores and throats. Consistent with the pore-filling sequence for a water-wet medium, as shown in Fig. 9, when the fractional flow increased, we can see that brine initially filled the smaller elements, and then filled progressively larger pores and throats. Oil always occupied the larger pores and throats. When f_w increased from 0.05 to 0.7, brine mainly filled in more small pores and the corners of larger pores. More brine occupied pores of intermediate size when $f_w > 0.7$.

For comparison, Fig. 10 illustrates a different pore-throat filling sequence in the mixed-wet case. During the waterflooding process, there is no preference for the water to fill either large or small pores. This shows that local contact angle, rather than pore size, is the principal determinant of the filling sequence. There is, however, a tendency for the smaller throats to fill first, which indicates that the narrowest restrictions in the pore space remain largely water-wet after aging. Overall, more oil was displaced compared to the water-wet case, showing that mixed-wet conditions give a lower residual oil saturation (Alhammadi et al., 2017; Jadhunandan and Morrow, 1995).

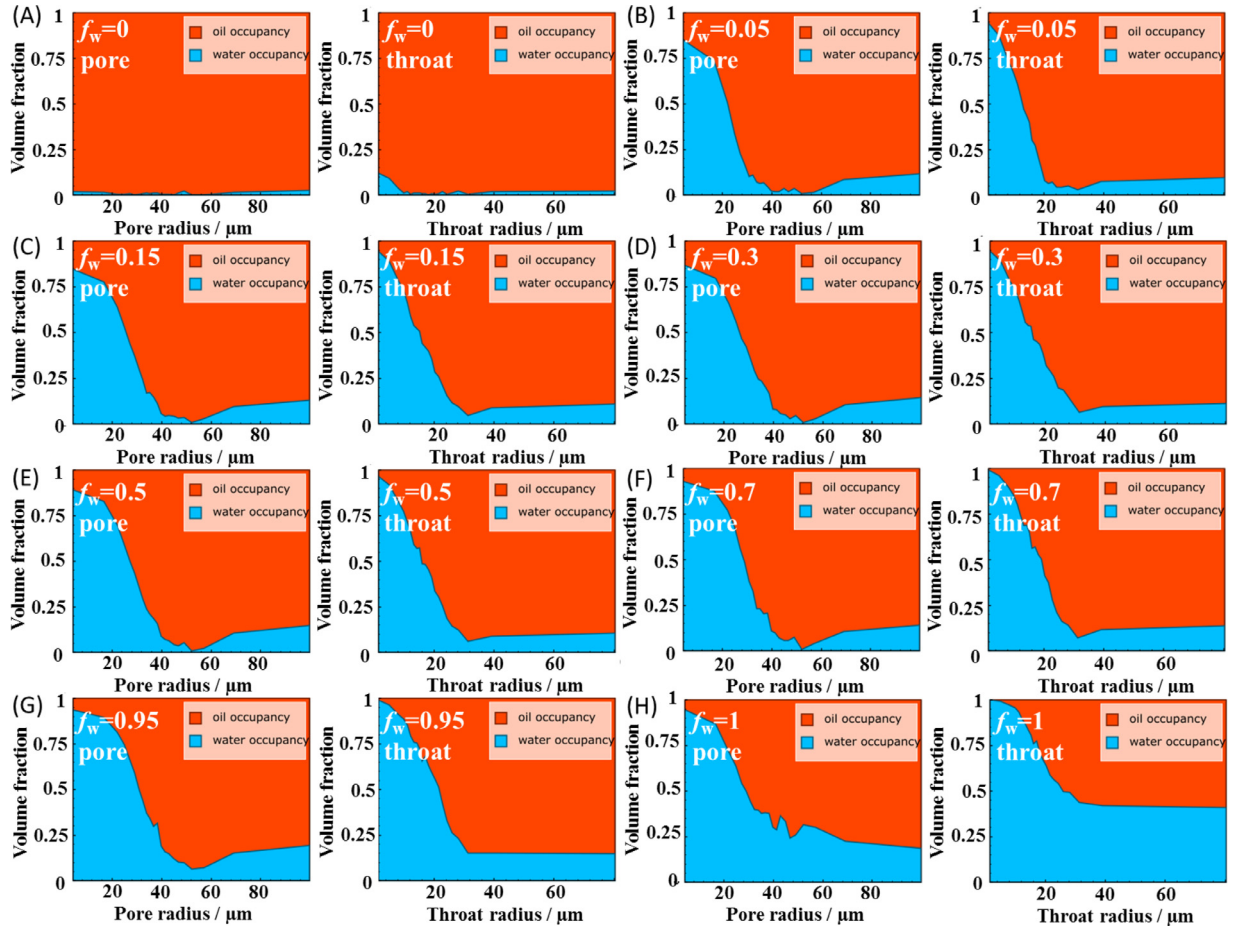


Fig. 9. The volume fraction of pore/throat radii occupied by oil (red) and brine (blue) as a function of radius under water-wet conditions for eight fractional flows.

To quantify the correlation between the radius of pore space, oil occupancy and filling order, we calculate the Pearson correlation coefficient (Benesty et al., 2009) for the water-wet and mixed-wet samples. The Pearson correlation coefficients between oil occupancy at pore and throat centres (which is either 1 or 0) and their inscribed radii for each fractional flow are shown in Fig. 11. The correlation coefficient is computed with pore and throat volumes as weighting factors:

$$CC = \frac{Cov(r, a)}{\sigma_r \sigma_a} \quad (2)$$

where $Cov(r, a) = \sum_i v_i(a_i - \bar{a})(r_i - \bar{r}) / \sum_i v_i$ is the covariance between radius (r) and oil occupancy (a) and $\sigma_x = \sqrt{Cov(x, x)}$ is the standard deviation, v is pore or throat volume and the summation is performed over all pores and throats (subscript i).

For the water-wet sample, the correlation coefficient initially increases with S_w and is approximately 0.6 when $S_w > 0.4$. However, for the mixed-wet experiment, the correlation coefficient decreases when S_w increases. The correlation between pore and throat radius and oil occupancy at the end of water-injection is 0.54 in the water-wet case while it is -0.06 for the mixed-wet data. We can conclude that there is a reasonably strong correlation between pore and throat radius and occupancy by oil for the water-wet sample, but essentially no correlation in the mixed-wet case. This proves that for the water-wet case, oil is first pushed out of small pores and then out of some large pores as well. In the altered wettability case, both small and large pores tend to be filled at low water fractional flows but overall more oil is displaced from large pores than out of smaller pores, and hence the correlation coefficients move toward zero and negative values as the fractional flow is increased.

3.3. Interfacial area

Fig. 12(A) shows the oil/brine interfaces at $f_w = 0.5$ for an image of size $560 \times 560 \times 560$ voxels with a voxel size of $3.58 \mu\text{m}$ as an example. The interfaces between oil and brine were extracted and smoothed using a volume preserving Gaussian smoothing to remove voxelization artefacts (Taubin, 1995). We can see that the interfaces are quasi-spherical in the water-wet case, while the arrangement of the interfaces is more complex for the mixed-wet experiment: we observe saddle-shaped interfaces with opposite curvatures in orthogonal directions. This will be discussed in more detail in Section 3.4.

The measured specific interfacial area, which is the interfacial area per unit volume, between oil-brine, brine-solid and oil-solid is shown in Fig. 12(B). For both cases, the interfacial area between oil and solid was highest at the beginning of the waterflood when oil occupied almost all the pore space.

For the water-wet case, at higher water saturations, brine starts to fill small pores and the corners of large pores and the water-solid interfacial area increased approximately linearly with water saturation, while the oil-solid interfacial area decreased correspondingly. The oil-brine interfacial area increased first and reached a maximum at $f_w = 0.7$, then decreased at higher fractional flows. The menisci between oil and brine contributing to the area principally block pores and throats and add to the resistance to flow. At higher fractional flows the oil-brine area decreases as there are fewer menisci, although it remains high, as oil is trapped in the larger pore spaces surrounded by brine.

For the mixed-wet case, the oil-solid interfacial area initially decreases rapidly, which represents the displacement of oil from some of the larger pores. The final area at the end of waterflooding is lower

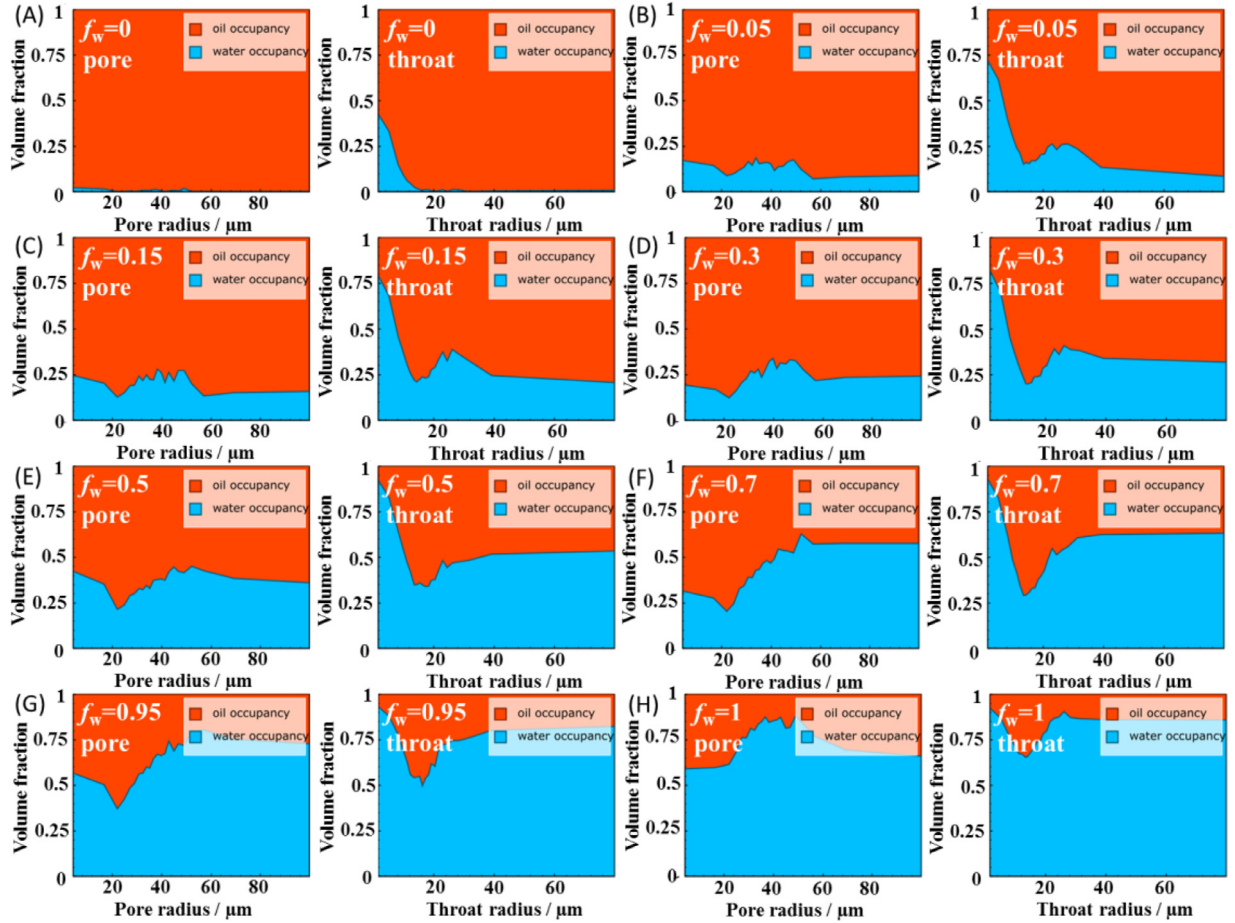


Fig. 10. The volume fraction of pore/throat radii occupied by oil (red) and brine (water) as a function of radius in the reservoir sandstone under mixed-wet conditions for eight fractional flows.

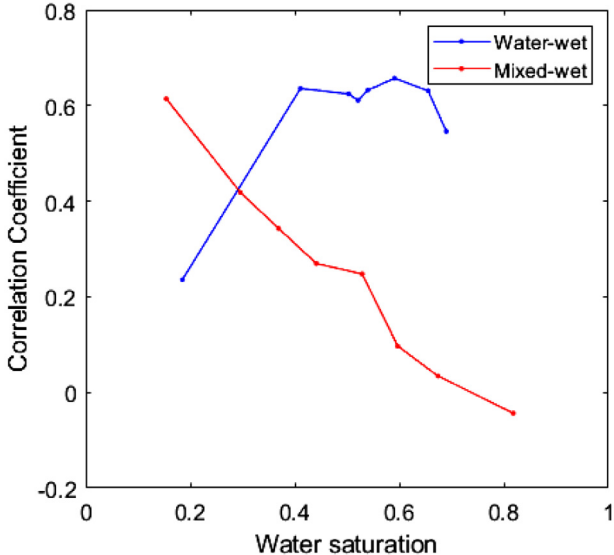


Fig. 11. Pearson correlation coefficients, Eq. (2), between oil occupancy at pore and throat centres and their inscribed radii as a function of saturation under water-wet and mixed-wet conditions.

than in the water-wet case, since the remaining oil saturation is lower. The oil-brine interfacial area increased initially with fractional flow and reached a maximum at $f_w = 0.5$, then decreased. The maximum oil-water interfacial area was approximately 50% larger in the mixed-wet

case, which is consistent with the visualizations in Fig. 12(A), showing sheet or saddle-like menisci spanning the sample.

3.4. Curvature analysis

The Gaussian curvature is defined as $K = \kappa_1 \kappa_2$ (Berger and Gostiaux, 2012; Gauss and Pesic, 2005) where κ_1 and κ_2 are the two principal curvatures and we define $\kappa_1 \geq \kappa_2$. The mean curvature is $\kappa = (\kappa_1 + \kappa_2)/2$. Both mean and Gaussian curvatures were analysed on the same sub-volume considered for interfacial area in the previous section. The mean curvature was measured on the connected oil phase and brine clusters of volume greater than 0.01 mm^3 . In the water-wet case, the curvature values larger than $0.2 \mu\text{m}^{-1}$ or smaller than $-0.2 \mu\text{m}^{-1}$ were considered as outliers caused by segmentation artefacts and were excluded from the analysis (Alhammadi et al., 2020; Lin et al., 2018; 2019). In the mixed-wet case, curvature values larger than $0.25 \mu\text{m}^{-1}$ or smaller than $-0.25 \mu\text{m}^{-1}$ were excluded.

Fig. 13 illustrates the mean curvature distribution at $f_w = 0.5$ for both cases where we identify three possibilities: $\kappa_1 < 0, \kappa_2 < 0$; $\kappa_1 \kappa_2 \leq 0$ and $\kappa_1 > 0, \kappa_2 > 0$. The mean curvature distribution includes measurements for both connected and disconnected oil-brine interfaces.

In the water-wet case, most interfaces have two positive principal curvatures, although in many cases one curvature is positive and the other negative – this represents arc menisci in the corners of the pore space (Andrew et al., 2014a). The percentage of the principal curvature groups defining different Gaussian curvatures that have both positive, both negative, and one positive/one negative principal curvatures is 58.8%, 0.2% and 41.0% respectively. The interfaces with one positive curvature and the other negative are important to maintain con-

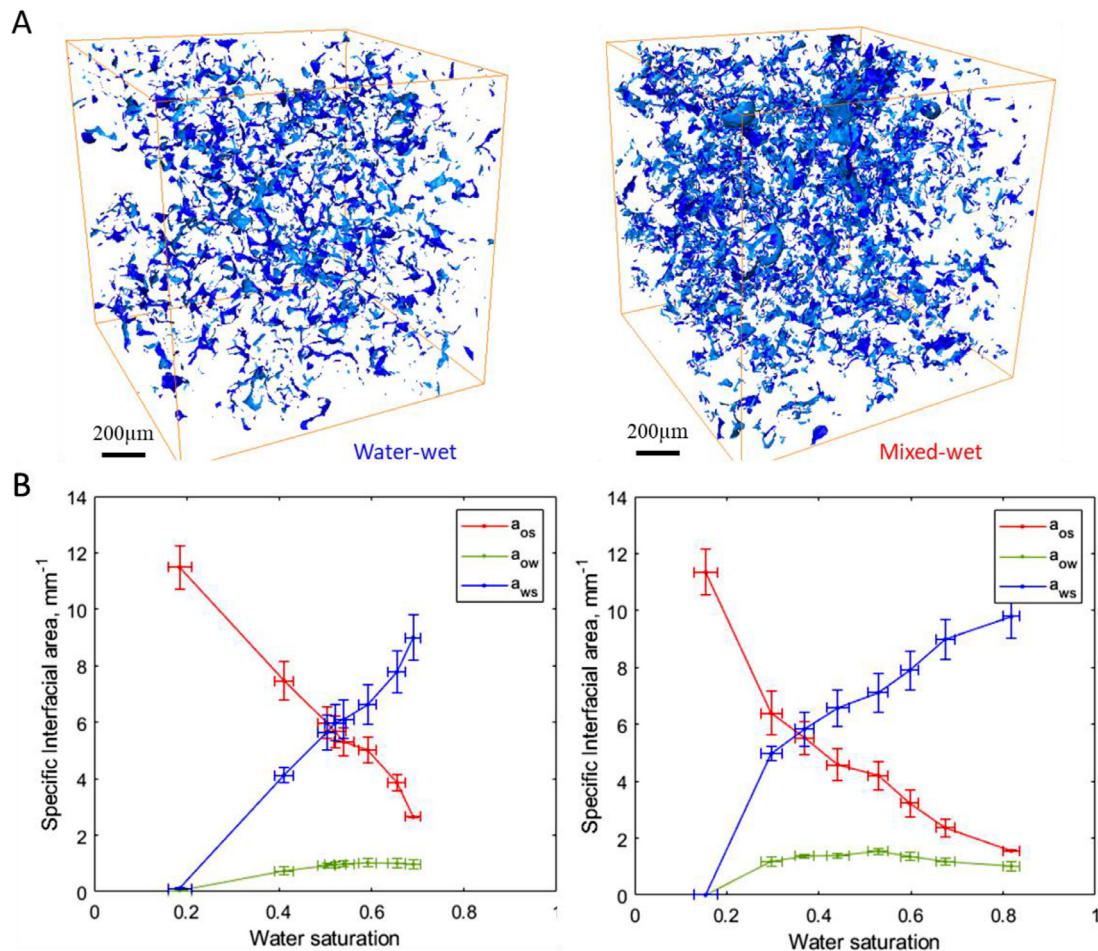


Fig. 12. (A) Oil-brine interface extraction based on three-phase segmentation in the water-wet (left) and mixed-wet (right) experiments on the same reservoir sandstone. (B) Oil-solid, oil-brine and brine-solid specific interfacial areas, a_{os} , a_{ow} and a_{ws} respectively, as a function of water (brine) saturation.

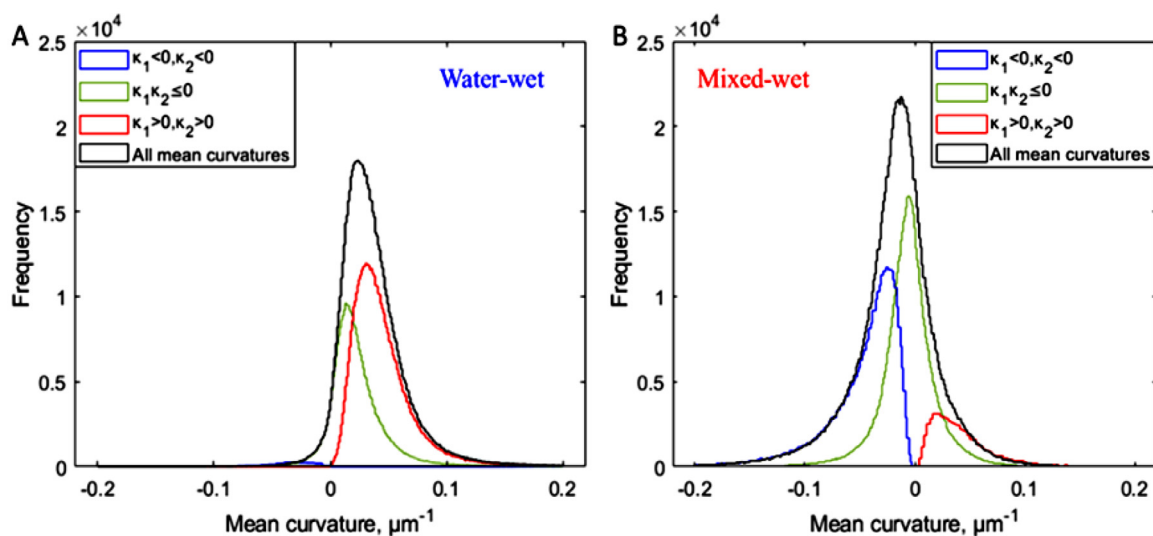


Fig. 13. Measured oil-brine mean curvature distribution for water-wet and mixed-wet interfaces at $f_w=0.5$. All mean curvatures are shown in black. The distribution of values where both principal curvatures are positive (red), $\kappa_1 > 0, \kappa_2 > 0$, both negative (blue), $\kappa_1 < 0, \kappa_2 < 0$, and when one value is positive and the other negative (green), $\kappa_1 \kappa_2 < 0$. The mean curvatures were measured using all oil-brine interfaces.

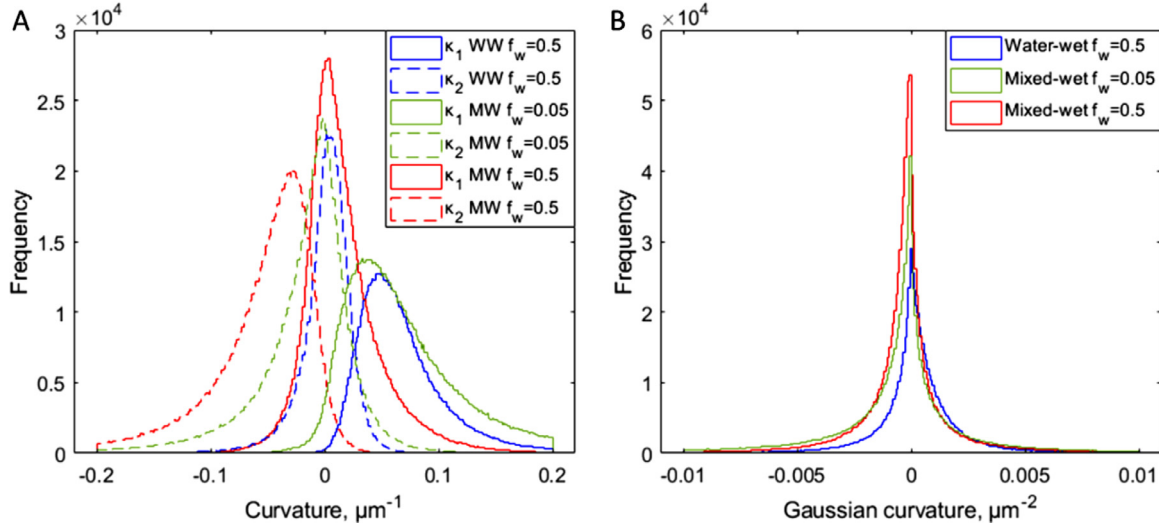


Fig. 14. Distribution of the two principal curvatures κ_1 and κ_2 and the Gaussian curvature for water-wet ($f_w=0.5$) and mixed-wet ($f_w=0.05$ and 0.5) reservoir sandstone. Both curvatures were measured using the connected oil phase only.

nectivity of the oil, as discussed later. There are almost no interfaces with two negative principal curvatures, indicating that water is well connected.

In the mixed-wet experiment, there are more negative curvatures than positive curvatures, and most of the curvatures have one positive and one negative value, giving a negative Gaussian curvature. The percentage of the principal curvature groups, that have both positive, both negative, and one positive/one negative principal curvatures is 3.9%, 32.8%, and 63.3% respectively. As we show later this has implications for oil connectivity. There are more interfaces that have two negative principal curvatures than the ones that have two positive curvatures. This implies poor water connectivity but better oil connectivity, signifying a lower residual oil saturation.

Fig. 14(A) shows the distributions of the two principal curvatures κ_1 and κ_2 for the water-wet experiment at $f_w=0.5$ and for the mixed-wet experiment at $f_w=0.05$ and $f_w=0.5$. Fig. 14(B) shows the corresponding Gaussian curvatures for the connected oil phase. Both κ_1 and κ_2 distributions are more negative in the mixed-wet case. For the water-wet case at $f_w=0.5$, κ_1 is always positive while κ_2 has both negative and positive values. For the mixed-wet case both κ_1 and κ_2 shift towards more negative values from the $f_w=0.05$ to $f_w=0.5$. This difference in principal curvatures for $f_w=0.05$ and $f_w=0.5$ is sufficiently large that, as we will show in Section 3.5, for the former this results in a positive mean curvature and hence positive capillary pressure, while for the latter capillary pressure is negative. Moreover, the distributions are wider in the mixed-wet case implying more negative Gaussian curvatures leading to simultaneous flow of oil and brine, as shown in Fig. 14(B).

Fig. 15 shows the mean curvature for all eight fractional flows. Here we consider the connected oil phase only, which contributed to the flow. In the beginning of waterflooding, as brine preferentially filled more water-wet regions of the pore space, the shape of oil-brine menisci was almost spherical with a positive mean curvature. For the water-wet case, the mean curvatures for all fractional flows remained positive, consistent with previous experiments on water-wet Bentheimer sandstone (Lin et al., 2018). However, in the mixed-wet case, for $f_w \geq 0.3$, invasion principally filled oil-wet regions, where the thermodynamic contact angle for displacement was greater than 90°, see Fig. 8(C). As a result, the mean curvatures were negative, again as seen in a mixed-wet Bentheimer (Lin et al., 2019) and an aged reservoir carbonate (Alhammadi et al., 2020).

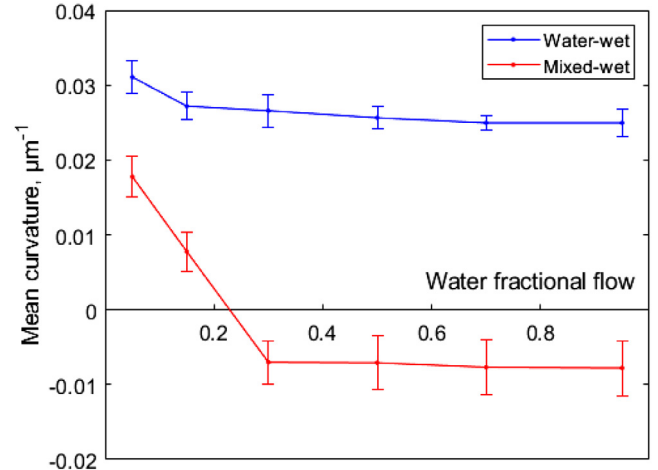


Fig. 15. Mean curvature as a function of water fractional flow under water-wet and mixed-wet conditions in the same reservoir sandstone. Mean curvatures were measured using the connected oil phase only.

Fig. 16 demonstrates the average Gaussian curvature for the eight fractional flows by considering all the interfaces between oil and brine. As mentioned at the start of this section, Gaussian curvature is the product of the two principal curvatures in orthogonal directions.

The Gauss-Bonnet theorem provides a relationship between the topology of the oil clusters and the integral of the Gaussian curvature across the bounding surface (Allendoerfer and Weil, 1943; Armstrong et al., 2019; Blunt et al., 2020): the more negative the value of this integral the better connected the object considered. Here connectivity refers to the number of redundant loops in the structure. In our context, for a negative Gaussian curvature, when water invades oil-occupied pores and throats, the oil remains connected, since filling does not disconnect the oil clusters.

In both cases, the Gaussian curvatures are negative with a similar magnitude when $f_w < 1$, which shows that the oil connectivity remains high even when more brine was injected into the sample. The absolute value of average Gaussian curvature obtained from the mixed-wet case was larger than that obtained from water-wet case, implying that the oil connectivity was better in mixed-wet case, as the oil can remain

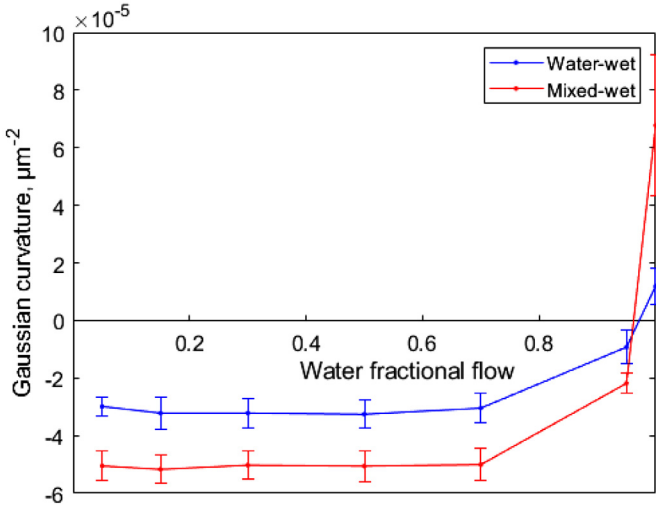


Fig. 16. Average Gaussian curvature as a function of water fractional flow under water-wet and mixed-wet conditions for the same reservoir sandstone. Gaussian curvatures were measured using all oil-brine interfaces.

in layers even in water-occupied pores and throats, which is consistent with a lower residual oil saturation. At $f_w = 1$, the end point, the oil is disconnected and hence trapped and, in both cases, the Gaussian curvature therefore is, as expected, positive. As Fig. 17(A) shows, the volume of trapped oil ganglia under water-wet conditions was larger than that under mixed-wet conditions, and this is supported by the ganglia size distribution analysis shown in Fig. 17(B). In the water-wet case we see fewer small trapped clusters and more larger clusters, as opposed to the mixed-wet system where the remaining oil resides in smaller pores and as layers.

3.5. Capillary pressure

Capillary pressure is defined as the pressure difference between the oil and brine phases: $P_c = P_o - P_w$. The local capillary pressure has been calculated from mean interfacial curvature from pore-scale images, Section 3.4, using the Young-Laplace law:

$$P_c = 2\sigma\kappa. \quad (3)$$

The capillary pressure calculated from Eq. (3), using the mean curvature shown in Fig. 15, is illustrated in Fig. 18. The uncertainties in saturation are estimated from likely uncertainties in the image segmentation. The uncertainties in capillary pressure are calculated from the variations in the mean interfacial curvature.

For the water-wet case, the capillary pressure is positive and gradually decreases with saturation. Here oil is displaced from water-wet pores by spontaneous imbibition. For the mixed-wet case, capillary pressure becomes negative signifying water injection for which water needs to be forced into more oil-wet pores, resulting in additional recovery. The primary drainage capillary pressure was measured on a separate sample taken from the same larger block of sandstone as the one used in these experiments.

3.6. Relative permeability

Darcy's law was used to calculate the relative permeabilities for the sample under water-wet and mixed-wet conditions. The brine saturation at each fractional flow was measured from the images of the whole sample, see Fig. 1. The brine saturation profiles measured across the whole sample for all fractional flows are shown in Fig. 19. This accounts for both brine in the macro-pores, explicitly resolvable in the segmented images, and brine in micro-porosity – see Section 2.3.2. Fig. 19(A1) and

(B1) shows the brine saturation profiles averaged in slices perpendicular to the flow direction for all the eight fractional flows over the length of the whole image taken with a voxel size of $6.35 \mu\text{m}$ under water-wet and mixed-wet conditions, respectively. For comparison, Fig. 19(A2) and (B2) shows the brine saturation profiles over the part of the sample scanned with the voxel size of $3.58 \mu\text{m}$ under water-wet and mixed-wet conditions, respectively. Since there is no discernible saturation gradient, we do not correct for the capillary pressure gradients caused by capillary end effect (Lin et al., 2019), which is not unexpected in systems with low capillary pressure.

The pressure differentials across the sample at steady-state were recorded by a precise differential transducer (PD-33X, Keller) with a range of 500 kPa, and the accuracy was 0.05% of the whole range. Table 4 presents the pressure differential and its standard deviation for both water-wet and mixed-wet experiments. The relative permeabilities were calculated by:

$$k_{rw} = \frac{q_w \mu_w L}{\Delta p K}; k_{ro} = \frac{q_o \mu_o L}{\Delta p K}, \quad (4)$$

where k_r is the relative permeability of each phase, q is the Darcy velocity of each phase, μ is the viscosity, L is the length of the whole sample, Δp is the pressure differential along the sample and K is the absolute permeability. The subscript w represents the brine (water) phase and o represents the oil. Table 4 presents the brine (water) saturation and the relative permeabilities at each fractional flow for these two experiments.

Fig. 20 shows the measured relative permeabilities for the same sample under water-wet and mixed-wet conditions. Error bars in the x-direction consider uncertainties caused by segmentation. Error bars in the y-direction consider uncertainties caused by the measurement of the length and diameter, pressure measurement and the pump rates. In the water-wet case, the initial water saturation was 0.20. In the mixed-wet case, the initial water saturation was 0.17. In both cases the initial water principally resides in sub-resolution micro-porosity, see Section 2.3.2.

Initially ($f_w = 0$), k_{ro} is slightly higher in the mixed-wet case. However, during displacement, at the same fractional flow between 0.15 and 0.95, both water and oil relative permeabilities in the mixed-wet case are lower than those in water-wet case. Menisci spanning the pore space impede the flow of the fluids – the lower relative permeabilities in the mixed-wet case are consistent with the larger oil-brine interfacial areas measured, see Fig. 12. While, in the mixed-wet case, brine occupies some of the larger pores, Fig. 10, these pores do not connect across the pore space until a high brine saturation is reached, which keeps the water relative permeability low. The oil relative permeability is also low, as the oil now is confined to smaller pores. These results are consistent with previous measurements on a mixed-wet Bentheimer sandstone (Lin et al., 2019) and a reservoir carbonate (Alhammadi et al., 2020).

At the end point ($f_w = 1$), k_{rw} in the mixed-wet case with a residual oil saturation of 0.18 is higher than that in water-wet case which has a higher residual oil saturation of 0.26; this is consistent with the connectivity analysis based on Gaussian curvature, Fig. 16, that indicates that the oil is better-connected in the mixed-wet case. The water tends to occupy some of the larger pores, particularly near the end point, as seen in Fig. 10, which explains the higher end-point water relative permeability, compared to the water-wet experiment, where water only resides in the smaller pores, see Fig. 9.

Our results are compared with the experimental results obtained from Bentheimer sandstone under water-wet conditions by Gao et al. (2017) and Lin et al. (2018; 2019) under both water-wet and mixed-wet conditions. Bentheimer has a similar pore structure, porosity and permeability to the reservoir sample here, although it contains a negligible amount of micro-porosity. These results show similar trends for both the water-wet and mixed-wet cases. There is, however, one crucial difference. In Bentheimer, the cross-over saturation, where the two relative permeabilities are equal, in the mixed-wet case was higher, implying – in mainly cases – a more favourable waterflood oil recovery (Blunt, 2017). In our experiments the water saturation of the cross-over

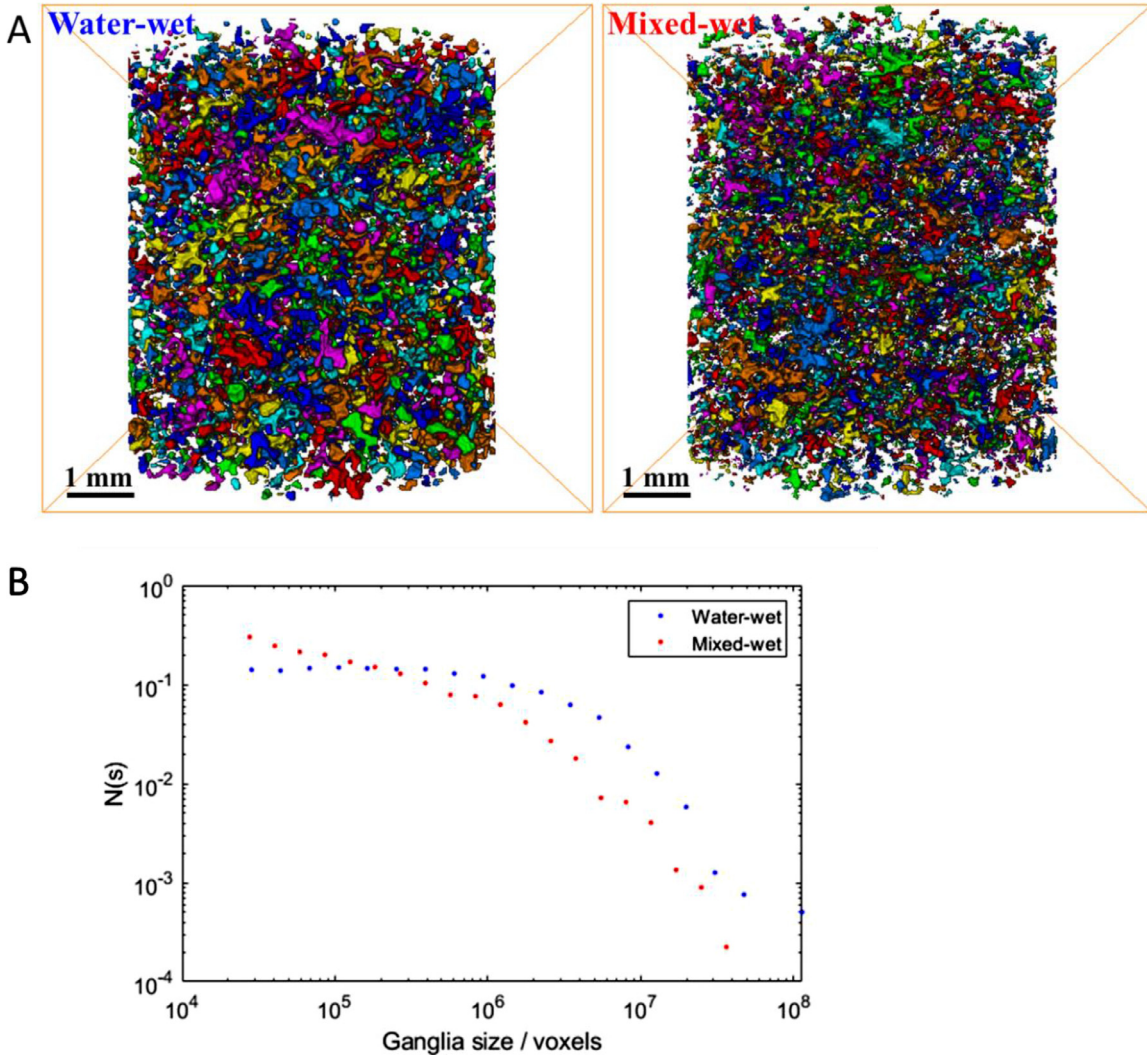


Fig. 17. (A) Three-dimensional images of oil clusters at $f_w = 1$ under water-wet and mixed-wet conditions. Each cluster is given a different colour. (B) Ganglia size distribution at $f_w = 1$ under water-wet and mixed-wet conditions.

Table 4
Brine (water) saturation, relative permeabilities and pressure differentials of the eight fractional flows under water-wet and mixed-wet conditions.

f_w	Water-wet				Mixed-wet			
	S_w	K_{ro}	K_{rw}	$\Delta p/kPa$	S_w	K_{ro}	K_{rw}	$\Delta p/kPa$
0	0.20	0.620	0	2.16 ± 0.12	0.17	0.677	0	1.99 ± 0.01
0.05	0.44	0.137	0.002	9.26 ± 0.16	0.37	0.135	0.002	9.60 ± 0.01
0.15	0.50	0.068	0.004	16.59 ± 0.18	0.45	0.036	0.003	32.11 ± 0.01
0.3	0.55	0.046	0.006	20.29 ± 0.29	0.50	0.022	0.004	42.29 ± 0.02
0.5	0.59	0.038	0.012	17.42 ± 0.84	0.54	0.013	0.005	51.21 ± 0.04
0.7	0.63	0.031	0.023	13.60 ± 1.09	0.62	0.007	0.006	53.88 ± 0.03
0.95	0.69	0.011	0.066	6.41 ± 0.61	0.66	0.004	0.022	18.01 ± 0.01
1	0.74	0	0.111	3.80 ± 0.04	0.82	0	0.191	2.19 ± 0.01

point is similar under both conditions. This cross-over is governed by a subtle balance of pore occupancy and connectivity, controlled by pore structure and wettability. In Bentheimer, the water filled some larger pores under mixed-wet conditions, but these pores remained poorly connected. In our experiments, we observe the same phenomenon, but the water relative permeability rises slightly more rapidly. This is likely due to increases in connectivity and conductivity mediated by the small amount of water-filled micro-porosity, which is absent in Bentheimer.

4. Conclusions

To assess the impact of wettability on two-phase flow signatures in porous media, we combined micro-CT imaging with a waterflood experiment, and conducted steady-state measurements on one reservoir sandstone sample under both water-wet and mixed-wet conditions. The comparison of wettability, pore occupancy, interfacial area, mean curvature, Gaussian curvature, capillary pressure and relative permeability in the same rock sample allows us to obtain a rich understanding of the

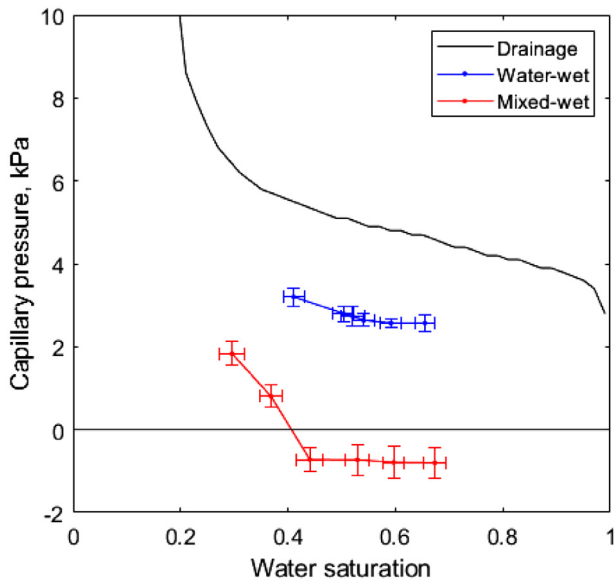


Fig. 18. The capillary pressure as a function of saturation estimated from the mean interfacial curvature of connected phases as a function of water (brine) saturation. The capillary pressure at the starting point of $f_w = 0$ are not shown as there are no interfaces observable in the pore-scale image. The capillary pressure at the end point of $f_w = 1$ is also not shown, as the oil phase is disconnected across the subvolume. The capillary pressure for primary drainage rescaled from mercury injection measurements is shown by the black line.

two-phase displacement mechanisms and changes in pore occupancy caused by wettability alteration.

1. The measured average of geometric contact angles was within the range of 74° - 76° under water-wet conditions while it was 88° - 91° for mixed-wet conditions. The thermodynamic contact angle, computed for displacement using energy balance, was approximately 65° in the water-wet case but 116° in the mixed-wet sample at the end of the displacement.
2. Brine mainly filled small pores and throats and the corners of larger pores and oil occupied the large pores for the water-wet

case, while pores of all size were filled during waterflooding in the mixed-wet case.

3. For both water-wet and mixed-wet experiments, with an increase in water fractional flow, the oil-brine interfacial area increased, reached a maximum value and then decreased. The oil-brine interfacial area was 50% larger in the mixed-wet case, implying greater blocking of the pore space by menisci.
4. The mean curvatures for the connected oil phase were positive in the water-wet case, while they were positive at the start of waterflooding and then became negative for fractional flows $f_w \geq 0.15$ in the mixed-wet experiment, as more oil-wet regions of the pore space were invaded.
5. The average Gaussian curvatures, defined as the product of the two principal curvatures, was negative during the displacement, implying connected phases. The Gaussian curvature was lower (more negative) in the mixed-wet case, which explains the better connectivity of the oil phase and the lower residual oil saturation.
6. Capillary pressure was calculated from the mean interfacial curvature. For the water-wet case, capillary pressures were positive and decreased slowly with an increase of f_w . For the mixed-wet case, capillary pressures were positive at the start and became negative when $f_w \geq 0.15$.
7. Relative permeabilities were calculated from the pressure differential measured during the experiment and the saturation calculated based on the images. Consistent with the analysis of pore occupancy and interfacial area, the relative permeabilities for the mixed-wet case were lower for the same fractional flow. The water relative permeability in the mixed-wet case remained low at intermediate saturation since the water, even if it resided in some of the larger pores, did not have connected pathways of wide pores through the pore space. At a higher water saturation, the water relative permeability rose to a higher value than in the water-wet case where the water was always confined to the smaller pores and throats. The oil relative permeability in the mixed-wet case was low since now oil occupied some of the smaller pores and throats with low conductance.

This imaging, experimental and analysis approach provides rich data sets to understand two-phase flow through porous media. The results can be used to benchmark and validate pore-scale models in the future. This method can be further applied in more heterogeneous rocks and

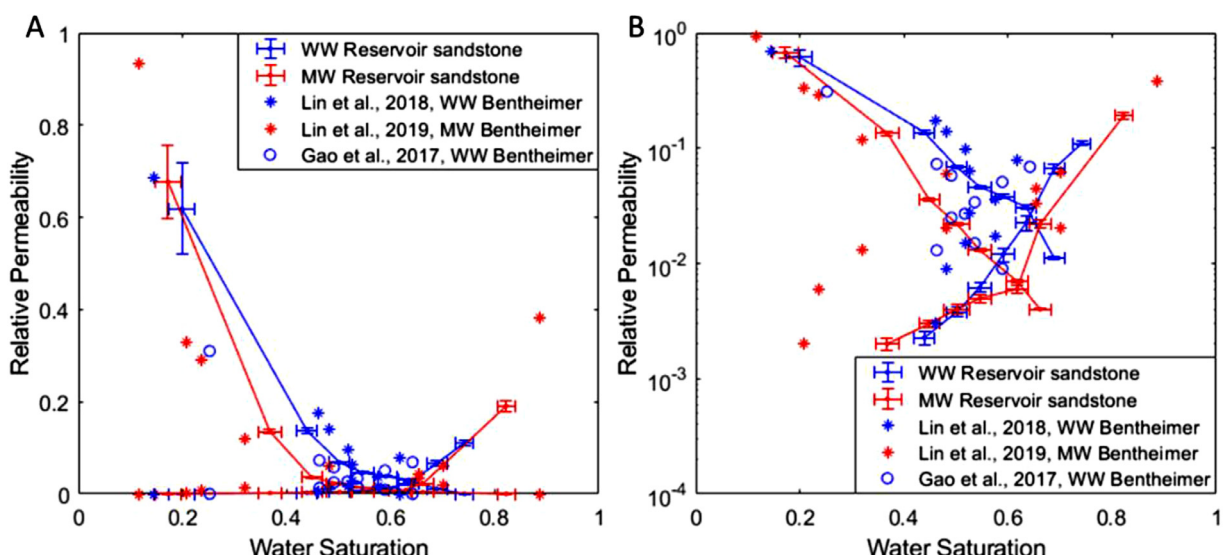


Fig. 20. Relative permeability measured for the steady-state oil-brine waterflooding experiments in the same sample under both water-wet (WW, blue) and mixed-wet (MW, red) conditions: (A) Liner plot; (B) Log plot. The results are compared to the experimental data in Bentheimer by Gao et al. (2017) and Lin et al. (2018, 2019).

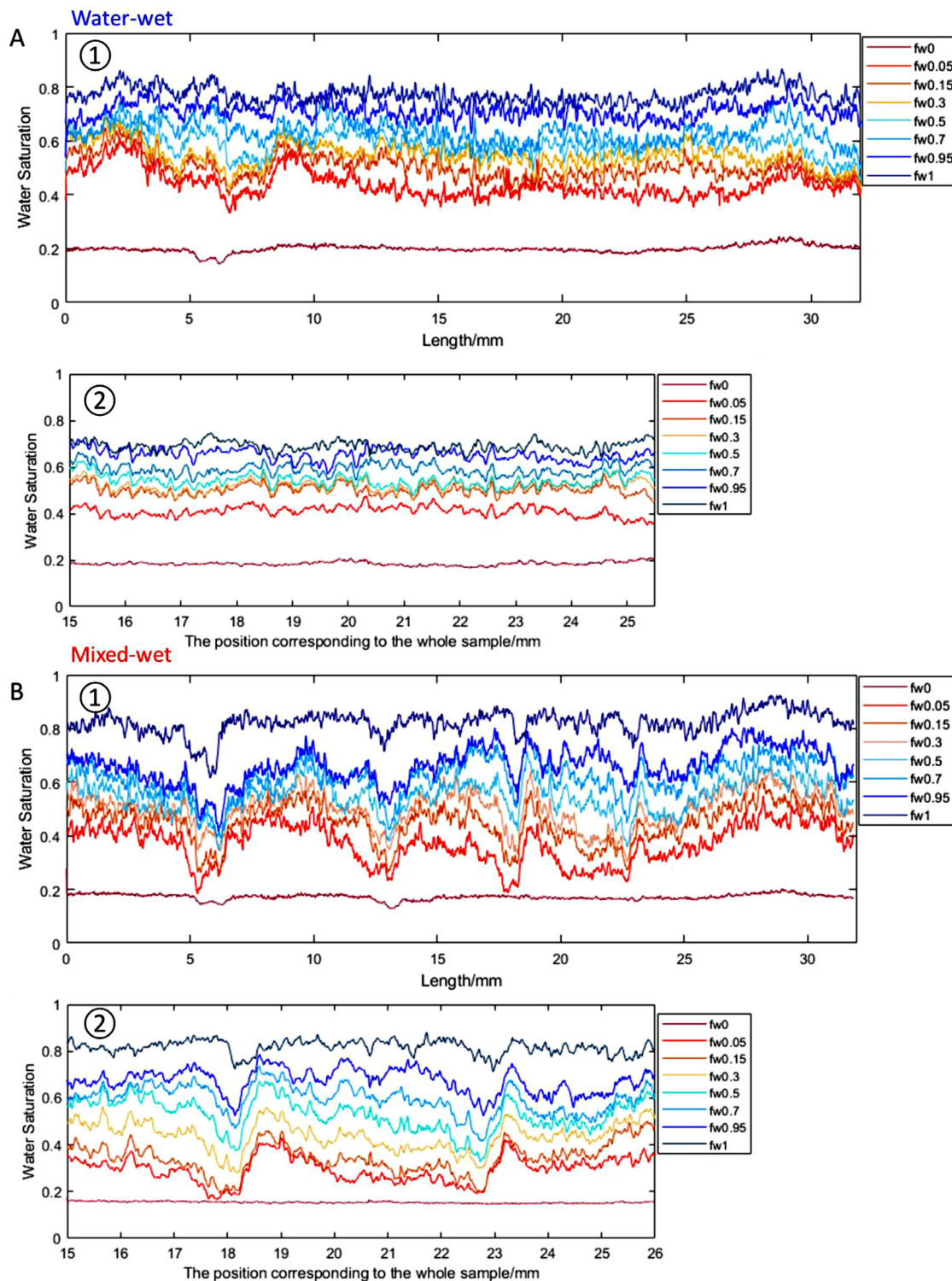


Fig. 19. Brine saturation profiles averaged in slices perpendicular to the flow direction for each of the eight fractional flows. (A1) Water-wet case over the length of the whole sample taken with a voxel size of $6.35 \mu\text{m}$. (A2) Water-wet case for the part of the sample scanned with a voxel size of $3.58 \mu\text{m}$. (B1) Mixed-wet case over the length of the whole sample taken with a voxel size of $6.35 \mu\text{m}$. (B2) Mixed-wet case for the part of the sample scanned with a voxel size of $3.58 \mu\text{m}$.

mixed-wet systems. Furthermore, this method can be applied to study various other porous medium problems, including fuel cells, water and vapour transport in plants, and carbon dioxide storage.

Declaration of Competing Interest

The authors declare that they have no known competing financial interests or personal relationships that could have appeared to influence the work reported in this paper.

CRediT authorship contribution statement

Ying Gao: Conceptualization, Investigation, Formal analysis, Writing - original draft, Writing - review & editing. **Ali Q. Raeini:** Investigation, Formal analysis, Writing - review & editing. **Ahmed M. Selem:** Investigation, Writing - review & editing. **Igor Bondino:** Conceptualization. **Martin J. Blunt:** Conceptualization, Supervision, Writing - review & editing. **Branko Bijeljic:** Conceptualization, Supervision, Writing - review & editing.

Acknowledgements

We would like to thank TOTAL for financial support and permission to publish this paper. BB is also very grateful to TOTAL for funding his Senior Fellowship.

References

- Akai, T., Alhammadi, A.M., Blunt, M.J., Bijeljic, B., 2019. Modeling oil recovery in mixed-wet rocks: pore-scale comparison between experiment and simulation. *Transp. Porous Media* 127 (2), 393–414. <https://doi.org/10.1007/s11242-018-1198-8>.
- Akai, T., Lin, Q., Bijeljic, B., Blunt, M.J., 2020. Using energy balance to determine pore-scale wettability. *J. Colloid Interface Sci.* <https://doi.org/10.1016/j.jcis.2020.03.074>.
- Alhammadi, A.M., AlRatrouf, A., Singh, K., Bijeljic, B., Blunt, M.J., 2017. In situ characterization of mixed-wettability in a reservoir rock at subsurface conditions. *Sci. Rep.* 7 (1), 10753. <https://doi.org/10.1038/s41598-017-10992-w>.
- Alhammadi, A.M., Gao, Y., Akai, T., Blunt, M.J., Bijeljic, B., 2020. Pore-scale X-ray imaging with measurement of relative permeability, capillary pressure and oil recovery in a mixed-wet micro-porous carbonate reservoir rock. *Fuel* 268, 117018. <https://doi.org/10.1016/j.fuel.2020.117018>.
- Allendoerfer, C.B., Weil, A., 1943. The gauss-bonnet theorem for riemannian polyhedra. *Trans. Am. Math. Soc.* 53 (1), 101–129.
- AlRatrouf, A., Raeini, A.Q., Bijeljic, B., Blunt, M.J., 2017. Automatic measurement of contact angle in pore-space images. *Adv. Water Resour.* 109, 158–169. <https://doi.org/10.1016/j.advwatres.2017.07.018>.
- AlRatrouf, A., Blunt, M.J., Bijeljic, B., 2018. Wettability in complex porous materials, the mixed-wet state, and its relationship to surface roughness. *Proc. Natl. Acad. Sci.* 115 (36), 8901LP–898906. <https://doi.org/10.1073/pnas.1803734115>.
- Anderson, W.G., 1987a. Wettability literature survey-part 6: the effects of wettability on waterflooding. *J. Petroleum Technol.* 39 (12), 1605–1622. <https://doi.org/10.2118/16471-PA>.
- Anderson, William G., 1987b. Wettability literature survey part 5: the effects of wettability on relative permeability. *J. Petroleum Technol.* 39 (11), 1453–1468. <https://doi.org/10.2118/16323-PA>.
- Andreas, J.M., Hauser, E.A., Tucker, W.B., 1938. Boundary tension by pendant drops 1. *J. Phys. Chem.* 42 (8), 1001–1019.
- Andrew, M., Bijeljic, B., Blunt, M.J., 2014a. Pore-by-pore capillary pressure measurements using X-ray microtomography at reservoir conditions: curvature, snap-off, and remobilization of residual CO₂. *Water Resour. Res.* 50 (11), 8760–8774. <https://doi.org/10.1002/2014WR015970>.
- Andrew, M., Bijeljic, B., Blunt, M.J., 2014b. Pore-scale contact angle measurements at reservoir conditions using X-ray microtomography. *Adv. Water Resour.* 68, 24–31. <https://doi.org/10.1016/j.advwatres.2014.02.014>.
- Armstrong, R.T., Porter, M.L., Wildenschild, D., 2012. Linking pore-scale interfacial curvature to column-scale capillary pressure. *Adv. Water Resour.* 46, 55–62. <https://doi.org/10.1016/j.advwatres.2012.05.009>.
- Armstrong, R.T., McClure, J.E., Robins, V., Liu, Z., Arns, C.H., Schlüter, S., Berg, S., 2019. Porous media characterization using minkowski functionals: theories, applications and future directions. *Transp. Porous Media* 130 (1), 305–335. <https://doi.org/10.1007/s11242-018-1201-4>.
- Avraam, D.G., Payatakes, A.C., 1995. Flow regimes and relative permeabilities during steady-state two-phase flow in porous media. *J. Fluid Mech.* 293, 207–236. <https://doi.org/10.1017/S0022112095001698>.
- Avraam, D.G., Payatakes, A.C., 1999. Flow mechanisms, relative permeabilities, and coupling effects in steady-state two-phase flow through porous media. the case of strong wettability. *Ind. Eng. Chem. Res.* 38 (3), 778–786. <https://doi.org/10.1021/ie980404o>.
- Bachu, S., 2003. Screening and ranking of sedimentary basins for sequestration of CO₂ in geological media in response to climate change. *Environ. Geol.* 44 (3), 277–289. <https://doi.org/10.1007/s00254-003-0762-9>.
- Bakhshian, S., Hosseini, S.A., 2019. Pore-scale analysis of supercritical CO₂-brine immiscible displacement under fractional-wettability conditions. *Adv. Water Resour.* 126, 96–107.
- Bakhshian, S., Rabbani, H.S., Hosseini, S.A., Shokri, N., 2020. New insights into complex interactions between heterogeneity and wettability influencing two-phase flow in porous media. *Geophys. Res. Lett.* 47 (14) e2020GL088187.
- Benesty, J., Chen, J., Huang, Y., Cohen, I., 2009. Pearson correlation coefficient. In: *Noise Reduction in Speech Processing*. Springer, pp. 1–4.
- Berg, S., Ott, H., Klapp, S.A., Schwing, A., Neiteiler, R., Brussee, N., et al., 2013. Real-time 3D imaging of Haines jumps in porous media flow. *Proc. Natl. Acad. Sci.* 110 (10), 3755–3759. <https://doi.org/10.1073/pnas.1221373110>.
- Berger, M., Gostiaux, B., 2012. *Differential Geometry: Manifolds, Curves, and Surfaces: Manifolds, Curves, and Surfaces*, 115. Springer Science & Business Media.
- Beucher, S., Meyer, F., 1993. The morphological approach to segmentation: the watershed transformation. *Math. Morphol. Image Process.* 34, 433–481.
- Blunt, M.J., 2017. *Multiphase Flow in Permeable media: a Pore-Scale Perspective*. Cambridge University Press.
- Blunt, M.J., Akai, T., Bijeljic, B., 2020. Evaluation of methods using topology and integral geometry to assess wettability. *J. Colloid Interface Sci.* 576, 99–108. <https://doi.org/10.1016/j.jcis.2020.04.118>.
- Blunt, M.J., Bijeljic, B., Dong, H., Gharbi, O., Iglauder, S., Mostaghimi, P., et al., 2013. Pore-scale imaging and modelling. *Adv. Water Resour.* 51, 197–216. <https://doi.org/10.1016/j.advwatres.2012.03.003>.
- Blunt, M.J., Lin, Q., Akai, T., Bijeljic, B., 2019. A thermodynamically consistent characterization of wettability in porous media using high-resolution imaging. *J. Colloid Interface Sci.* 552, 59–65. <https://doi.org/10.1016/j.jcis.2019.05.026>.
- Buades, A., Coll, B., Morel, J.M., 2005. A non-local algorithm for image denoising. 2005 IEEE Computer Society Conference on Computer Vision and Pattern Recognition (CVPR'05) <https://doi.org/10.1109/CVPR.2005.38>.
- Buades, Antoni, Coll, B., Morel, J.-M., 2008. Nonlocal image and movie denoising. *Int. J. Comput. Vis.* 76 (2), 123–139. <https://doi.org/10.1007/s11263-007-0052-1>.
- Buckley, J.S., Liu, Y., Monsterlet, S., 1998. Mechanisms of wetting alteration by crude oils. *SPE J.* 3 (01), 54–61. <https://doi.org/10.2118/37230-PA>.
- Burger, W., Burge, M.J., 2016. *Digital Image processing: an Algorithmic Introduction Using Java*. Springer.
- Gao, Y., Lin, Q., Bijeljic, B., Blunt, M.J., 2017. X-ray microtomography of intermittency in multiphase flow at steady state using a differential imaging method. *Water Resour. Res.* 53 (12), 10274–10292.
- Gao, Y., Qaseminejad Raeini, A., Blunt, M.J., Bijeljic, B., 2019. Pore occupancy, relative permeability and flow intermittency measurements using X-ray micro-tomography in a complex carbonate. *Adv. Water Resour.* 129, 56–69. <https://doi.org/10.1016/j.advwatres.2019.04.007>.
- Gao, Y., Lin, Q., Bijeljic, B., Blunt, M.J., 2020. Pore-scale dynamics and the multiphase Darcy law. *Phys. Rev. Fluids* 5 (1), 13801. <https://doi.org/10.1103/PhysRevFluids.5.013801>.
- Gauss, K.F., Pesic, P., 2005. *General Investigations of Curved Surfaces*. Courier Corporation.
- Herring, A.L., Harper, E.J., Andersson, L., Sheppard, A., Bay, B.K., Wildenschild, D., 2013. Effect of fluid topology on residual nonwetting phase trapping: implications for geologic CO₂ sequestration. *Adv. Water Resour.* 62, 47–58. <http://dx.doi.org/10.1016/j.advwatres.2013.09.015>.
- Hirasaki, G.J., 1991. Wettability: fundamentals and Surface Forces. *SPE Formation Eval.* 6 (02), 217–226. <https://doi.org/10.2118/17367-PA>.
- Jadhunandan, P.P., Morrow, N.R., 1995. Effect of wettability on waterflood recovery for crude-oil/brine/rock systems. *SPE Reservoir Eng.* 10 (01), 40–46. <https://doi.org/10.2118/22597-PA>.
- Khanamiri, H.H., Berg, C.F., Slotte, P.A., Schlüter, S., Torsæter, O., 2018. Description of free energy for immiscible two-fluid flow in porous media by integral geometry and thermodynamics. *Water Resour. Res.* 54 (11), 9045–9059. <https://doi.org/10.1029/2018WR023619>.
- Khishvand, M., Alizadeh, A.H., Oraki Kohshour, I., Piri, M., Prasad, R.S., 2017. In situ characterization of wettability alteration and displacement mechanisms governing recovery enhancement due to low-salinity waterflooding. *Water Resour. Res.* 53 (5), 4427–4443. <https://doi.org/10.1002/2016WR020191>.
- Kovscek, A.R., Wong, H., Radke, C.J., 1993. A pore-level scenario for the development of mixed wettability in oil reservoirs. *AIChE J.* 39 (6), 1072–1085. <https://doi.org/10.1002/aic.690390616>.
- Lin, Q., Al-Khalafi, Y., Blunt, M.J., Bijeljic, B., 2016. Quantification of sub-resolution porosity in carbonate rocks by applying high-salinity contrast brine using X-ray microtomography differential imaging. *Adv. Water Resour.* 96, 306–322. <http://dx.doi.org/10.1016/j.advwatres.2016.08.002>.
- Lin, Q., Bijeljic, B., Pini, R., Blunt, M.J., Krevor, S., 2018. Imaging and measurement of pore-scale interfacial curvature to determine capillary pressure simultaneously with relative permeability. *Water Resour. Res.* 54 (9), 7046–7060. <https://doi.org/10.1029/2018WR023214>.
- Lin, Q., Bijeljic, B., Pini, R., Blunt, M.J., Krevor, S., 2019. Minimal surfaces in porous media: pore-scale imaging of multiphase flow in an altered-wettability Bentheimer sandstone. *Phys. Rev. E* 99 (6), 63105. <https://doi.org/10.1103/PhysRevE.99.063105>.
- Morrow, N.R., 1970. Physics and thermodynamics of capillary action in porous media. *Ind. Eng. Chem.* 62 (6), 32–56. <https://doi.org/10.1021/ie50726a006>.

- Narula, C.K., Allison, J.E., Bauer, D.R., Gandhi, H.S., 1996. Materials chemistry issues related to advanced materials applications in the automotive industry. *Chem. Materials* 8 (5), 984–1003. <https://doi.org/10.1021/cm950588m>.
- Raeini, A.Q., Bijeljic, B., Blunt, M.J., 2017. Generalized network modeling: network extraction as a coarse-scale discretization of the void space of porous media. *Phys. Rev. E* 96 (1), 13312. <https://doi.org/10.1103/PhysRevE.96.013312>.
- Saif, T., Lin, Q., Gao, Y., Al-Khulaifi, Y., Marone, F., Hollis, D., et al., 2019. 4D in situ synchrotron X-ray tomographic microscopy and laser-based heating study of oil shale pyrolysis. *Appl. Energy* 235, 1468–1475. <https://doi.org/10.1016/j.apenergy.2018.11.044>.
- Salathiel, R.A., 1973. Oil recovery by surface film drainage in mixed-wettability rocks. *J. Petroleum Technol.* 25 (10), 1216–1224. <https://doi.org/10.2118/4104-PA>.
- Stauffer, C.E., 1965. The measurement of surface tension by the pendant drop technique. *J. Phys. Chem.* 69 (6), 1933–1938.
- Taubin, G., 1995. Curve and surface smoothing without shrinkage. In: Proceedings of IEEE International Conference on Computer Vision, pp. 852–857.
- Wildenschild, D., Sheppard, A.P., 2013. X-ray imaging and analysis techniques for quantifying pore-scale structure and processes in subsurface porous medium systems. *Adv. Water Resour.* 51, 217–246. <http://dx.doi.org/10.1016/j.advwatres.2012.07.018>.
- Zou, S., Armstrong, R.T., Arns, J., Arns, C.H., Hussain, F., 2018. Experimental and theoretical evidence for increased ganglion dynamics during fractional flow in mixed-wet porous media. *Water Resour. Res.* 54 (5), 3277–3289.